Volumetric Compression Induces Intracellular Crowding to Control Intestinal Organoid Growth via Wnt/#-Catenin Signaling

HHS Public Access

Author manuscript

Cell Stem Cell. Author manuscript; available in PMC 2022 January 07.

Published in final edited form as:

Cell Stem Cell. 2021 January 07; 28(1): 63–78.e7. doi:10.1016/j.stem.2020.09.012.

Volumetric compression induces intracellular crowding to control intestinal organoid growth via Wnt/β-catenin signaling

Yiwei Li[1,#], **Maorong Chen**[2,#], **Jiliang Hu**[1], **Ren Sheng**[2,3], **Qirong Lin**[1], **Xi He**[2], **Ming Guo**[1,4,*]

[1]Department of Mechanical Engineering, Massachusetts Institute of Technology, Cambridge, MA 02139, USA

[2]F. M. Kirby Center, Boston Children's Hospital, Harvard Medical School, Boston, MA 02115, USA

[3]College of life and health science, Northeastern University, Shenyang, Liaoning, 110004, China

[4]Lead Contact

Abstract

Enormous amounts of essential intracellular events are crowdedly packed inside picoliter-sized cellular space. However, the significance of the physical properties of cells remains underappreciated due to lack of evidence of how they impact cellular functionalities. Here, we show that the volumetric compression regulates the growth of intestinal organoids by modifying intracellular crowding and elevating Wnt/β-catenin signaling. Intracellular crowding varies upon stimulation by different types of extracellular physical/mechanical cues, and leads to a significant enhancement of Wnt/β-catenin signaling by stabilizing the LRP6 signalosome. By enhancing intracellular crowding using osmotic and mechanical compression, we show that expansion of intestinal organoids was facilitated through elevated Wnt/β-catenin signaling and greater intestinal stem cells (ISCs) self-renewal. Our results provide an entry point for understanding how intracellular crowdedness functions as a physical regulator linking extracellular physical cues with intracellular signaling, and potentially facilitate the design of engineering approaches for expansion of stem cells and organoids.

Graphical Abstract

*Corresponding author. guom@mit.edu.

#These authors contributed equally to this work.

AUTHOR CONTRIBUTIONS

Conceptualization, Y.L., M.G., and M.C.; Project Administration, M.G.; Supervision, M.G. and X.H.; Methodology, Y.L., M.G., M.C. and X.H.; Investigation, Y.L. and M.C.; Formal Analysis, Y.L. and M.C.; Validation, M.C., R.S. and Q.L.; Software, J.H. and Y.L.; Resources, X.H. and M.G.; Writing-Original Draft, Y.L.; Writing-Review & Editing, M.G., M.C. and X.H.; Visualization, Y.L., M.G., and M.C.. Funding Acquisition, M.G. and X.H.

DECLARATION OF INTERESTS

The authors declare no competing interests.

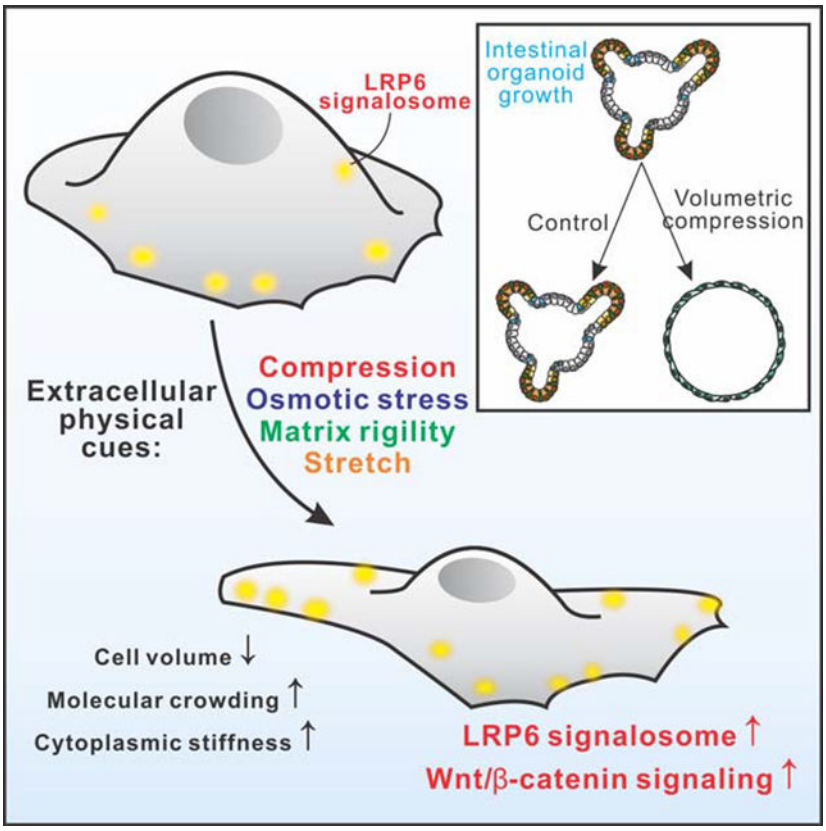

INTRODUCTION

A cell is the “building block of life” and a microscale structure (Bursac et al., 2005; Guo et al., 2014), with enormous amounts of macromolecules and biochemical processes tightly packed inside this picoliter-sized physical chamber (Zhou et al., 2008). Physical properties of the cell, including stiffness and intracellular crowding, change dynamically in response to varied extracellular cues, such as forces and osmotic stresses (Han et al., 2019; Li et al., 2020; Weng et al., 2016). However, the significance of these fundamental cellular physical properties remains largely unknown (Wirtz et al., 2011). Recent studies reveal that the physical condensation of chromatin determines the gene expression switch via mediating genome accessibility (Crowder et al., 2016; Eagen et al., 2015); moreover, cytoplasmic and nuclear phase transitions contribute to the organization of complex intracellular biochemical reactions in time and space (Shin et al., 2017; Strom et al., 2017). These findings highlight the fundamental role of the physical environment in regulating biological processes in the cell. In fact, all intracellular processes *in vivo* have evolved to function within crowded physical environments inside the cell rather than in dilute buffers (Guo et al., 2014; Zhou et al., 2008). Indeed, over the last few decades, molecular crowding has been considered as a critical factor affecting both the rate and equilibrium of interactions involving macromolecules, and the impact has been demonstrated in synthetic cellular systems (Hansen et al., 2016; Tan et al., 2013). A more recent study showed that crowding of the cytoplasm tuned by ribosomes increases intracellular phase separation (Delarue et al., 2018).

However, it remains elusive how intracellular physical characters, such as the crowdedness, affect signaling processes and physiological functionalities of mammalian cells (Ellis, 2001).

Tissues and organs are assembled spatiotemporally from cells under dynamic physical microenvironments (Serwane et al., 2017; Shyer et al., 2017; Xiong et al., 2014). For example, the self-renewing epithelium of the intestine is organized into crypts and villi (Sato et al., 2009); $Lgr5^+$ intestinal stem cells (ISCs) reside near the bottom of the crypt and rapidly generate new transit amplifying (TA) cells (Marshman et al., 2002). This expansion of proliferative $Lgr5^+$ ISCs induces mechanical stress at the bottom of the crypt (Sato and Clevers, 2013), and push TA cells towards the villus and decay along the crypt-villus axis (Batlle et al., 2002) (Fig. 1A). Meanwhile, the osmotic stress in intestine changes dynamically every day according to daily diet and digest (Overduin et al., 2014). Despite extensive studies of biochemical regulation in intestine (Farin et al., 2016), the impact of extracellular physical cues, which exhibit remarkable spatiotemporal heterogeneity, on functions of intestinal cells still remains elusive. It has been recently shown that high matrix stiffness enhanced ISC expansion in the content of ISC expansion medium using a synthetic matrix (Gjorevski, 2016). However, the effect of physical cues on intestinal crypts and crypt organoids in the physiological condition with endogenous Wnt concentration remains unknown. Moreover, how physical properties of cells regulate the physiological growth of this multicellular homeostasis remains largely unexplored.

Towards this end, we characterized the physical nature of intestinal epithelial cells and explored how cellular physical properties affect $Lgr5^+$ ISCs (Sato et al., 2009; Snippert et al., 2010) and Wnt/β-catenin signaling in both intestinal epithelium *in vivo* and organoids *ex vivo*. Furthermore, we investigated the underlying molecular processes, and our results suggest that the volumetric compression, induced by multiple extracellular physical cues (mechanical forces, matrix rigidity and osmotic stress), regulates Wnt/β-catenin signaling by modifying intracellular crowding. As demonstrated by both experimental measurements and numerical simulations, the increased intracellular crowding promotes the formation of LRP6 signalosomes via modulating equilibrium of LRP6-Axin binding, leading to further stabilization of β-catenin and a higher Wnt target gene expression. Our work demonstrates a crucial role for cellular physical properties in ISC self-renewing via maintaining its high response to Wnt ligands, revealing an unexpected ability of intracellular crowding to promote intestinal organoid growth.

RESULTS

Distinct physical properties of cells in intestinal epithelium

The self-renewing epithelium of intestine is organized into crypts and villi (Sato et al., 2009). Cells are newly generated from the bottom of crypts and undergo apoptosis at the tips of villi (Barker et al., 2007). The $Lgr5^+$ ISCs in the crypt divide and propel new cells along the crypt-villi axis to the tip (Batlle et al., 2002) (Fig. 1A). The compressive stress generated by cell expansion in crypt squeezes surrounding cells (Sato and Clevers, 2013). To characterize the physical heterogeneity in the intestinal epithelium, we imaged intestines from Lgr5-eGFP-IRES-CreERT2 mice (Barker et al., 2007) (Jackson Laboratory) *in situ* (Fig. 1B). We observed that $Lgr5^+$ ISCs were significantly smaller and thinner than the rest

Lgr5^{-} cells (Fig. 1B, C and Supplementary Fig. 1F), which is consistent with the long characterized thin morphology of ISCs (Barker and Clevers; Barker et al.; Cheng and Leblond, 1974). Then, we hypothesized that Lgr5^{+} ISCs might be distinguished from Lgr5^{-} cells by physical properties. To examine this, we measured both the aspect ratios and volumes of individual intestinal cells, including ISCs (Lgr5+), Paneth cells (LYZ+), +4 cells (Bmi1+) and TA cells (adjacent to crypt); we found that Lgr5^{-} cells had a larger volume and rounder morphology than ISCs (Fig. 1C, D and Supplementary Fig. 1A, F). Indeed, the aspect ratio of ISCs is 56.5% larger than Paneth cells, 25.6% larger than +4 cells, and similar to TA cells (Fig. 1D); this also suggests that physical properties could potentially serve as a morphological biomarker for ISCs. There are 14±2 ISCs in each crypt (Snippert et al., 2010), and when we choose the 14 smallest cells according to their volume in each crypt, 98% of chosen cells are positive for Lgr5 (Fig. 1K). Similar physical characters have also been used to distinguish subpopulations of embryonic stem cells (ESCs) and mesenchymal stem cells (Chowdhury et al., 2010; Lee et al., 2014). In addition, among all the lgr5− cells, Paneth cells are always larger and rounder than +4 cells and TA cells (Fig. 1B–D, and Supplementary Fig. 1F). We also measured the diffusion rate of free GFP in intestinal crypts by performing Fluorescent Recovery After Photobleaching (FRAP), which indicated the most crowded interior in Lgr5+ ISCs and the least crowded in Paneth cells (Supplementary Fig. 1G).

Furthermore, the nucleus of ISCs often had irregular shapes, such as triangles, rectangles and ellipses, while the nucleus of Paneth cells remained a round shape (Fig. 1E and Supplementary Fig. 1B, F). The major axial length of nuclei in ISCs were 47% longer than the diameter of nuclei in Paneth cells, 11% longer than +4 cells, and similar to TA cells (Fig. 1G). Interestingly, nuclei occupied a significantly larger cellular space in ISCs (58%±21%) as compared to Lgr5− cells (Fig. 1F); this is also consistent with the high nuclear to cytoplasmic ratio observed in ESCs, which is believed to indicate their high pluripotency (Stice et al., 1996).

The different morphologies between ISCs and Lgr5^{-} cells also suggested their possible different mechanical properties (Oakes et al., 2014; Tee et al., 2011). To test this, we applied uniaxial stretch to intestine tissue, and measured the resultant deformation of individual cells by imaging the transverse cross-section of crypts. The total engineering strain is obtained by the ratio of deformation divided by the initial length of the single crypt, in the direction of the applied force; meanwhile, the engineering strains of individual cells were measured (Fig. 1H). When a bulk strain of 60%±13% was applied to the crypt, the ISCs were deformed by only 9%±7%, while other Lgr5^{-} cells were deformed more significantly (Fig. 1I). We also replaced the medium with pure polyethylene glycol 300 (PEG 300) to osmotically compress the intestine; the ISCs reduced their volume by 41%±11% while the Paneth cells by 73% ±11%, the TA cells by 58±13%, and the +4 cells by 59±13% (Fig. 1J). These results indicate that the ISCs and their progeny cells respond differently upon physical stresses and have distinct mechanical properties.

Lgr5 serves as a marker to identify ISCs, and its relevant level of expression indicates corresponding stemness among ISC populations (Snippert et al., 2010). Here, we further queried whether there exists a relationship between the Lgr5 expression and its physical

properties in individual ISCs. Interestingly, we observed that the volume of individual ISCs was negatively correlated with its Lgr5 RNA expression level (Fig. 1L), suggesting potential interplays between physical properties and stemness of ISCs. Consistently, this correlation was also confirmed in cultured intestinal organoids *ex vivo* (Supplementary Fig. 1C–E).

Physical properties of intestinal cells correlate with Wnt/β-catenin signaling in crypts

Lgr5, known as a target gene of the Wnt/β-catenin pathway (Barker et al., 2007), masters the growth of intestinal epithelium and intestinal organoids. $Lgr5^+$ ISCs self-renews when it maintains high level Wnt/β-catenin signaling, while undergoes differentiation when the level is low (Farin et al., 2016). Thus we wonder if cellular physical properties work as a regulator of stemness of ISCs via modulating Wnt/β-catenin signaling. We stained β-catenin and found there was also a correlation between the β-catenin accumulation and cell volume in intestine (Fig. 1M, N). Among all four types of cells (Fig. 1O), there is no significant difference in average nuclear β-catenin in ISCs and Paneth cells (Fig. 1O); while, the TA cells and +4 cells have a much lower intensity of nuclear β-catenin. This observed trend of decaying nuclear β-catenin along the crypt-to-villi axis is consistent with previous studies (Van De Wetering et al., 2002; van Es et al., 2005), which is owing to the concentration of Wnt ligand gradient decreasing from crypt to villus. In crypt, Paneth cells serve as Wnt ligand resources to maintain a short-range gradient of Wnt ligands (Farin et al., 2016). When we plotted nuclear β-catenin intensity against their corresponding cell volume and aspect ratio respectively, we observed no obvious correlation (Fig. 1P, Q). These observed Wnt signaling activities are attributed to the concentration of Wnt ligands received by the cells, where the Paneth cells have the most Wnt ligands, then their adjacent ISCs and +4 cells. Moreover, ISCs and +4 cells are expected to receive the same amount of Wnt ligand as they are in direct contact with Paneth cells, among which we found that the smaller ISCs contain more nuclear β-catenin than the larger +4 cells (Fig. 1P, Q).

To exclude the effect of the varying amount of Wnt ligands, we treated the isolated intestinal crypts with the same amount of Wnt ligands in medium while inhibiting endogenous Wnt ligand secretion using IWP-2 compound (a porcupine inhibitor). After 1 day incubation, we stained and measured the nuclear β-catenin accumulation in all four types of intestinal cells. We observed that ISCs accumulate the largest amount of nuclear β-catenin, then +4 cells and TA cells, while Paneth cells the least (Fig. 1R). Additionally, the cell volume negatively correlates with nuclear β-catenin (with a linear regression of R^2=0.98) (Fig. 1S), while the cell aspect ratio positively correlated with nuclear β-catenin (with a linear regression of R^2=0.53) (Fig. 1T). Thus, we suspect that cell volume rather than cell aspect ratio might be a more dominant regulator of Wnt/β-catenin signaling.

Physical properties of cells correlate with Wnt/β-catenin signaling under various physical perturbations

To further investigate if changing cellular physical properties directly impact Wnt/β-catenin signaling, we manipulated the volume of individual human colon carcinoma RKO cells with hypertonic Wnt3a conditioned medium (Wnt3a-CM), which contained PEG 300, a polymer preventing non-specific protein binding (Akabayov et al., 2013). Indeed, we confirmed that PEG 300 does not interact with Wnt3a using a pull-down assay (Supplementary Fig. 1H).

RKO cells were selected to exclude the effect of cadherin-catenin association and its potential release of membrane β-catenin, since they do not express cadherin (Benham-Pyle et al., 2015; Jiang et al., 2018; Major et al., 2007). The volume of RKO cells was reduced by 22%±11% and 35%±19% under two hypertonic conditions with 1% and 2% PEG 300 (363 and 400 mOsm), respectively, as compared to those in isotonic media (0% PEG, 325 mOsm) (Fig. 2A, B). To monitor Wnt/β-catenin signaling, we measured the TOP-Flash reporter, a luciferase reporter assay that be used to monitor the strength of Wnt/β-catenin signaling (Biechele and Moon, 2008). Using this assay, we found that the TOP-flash signal increased by 1.99±0.14 and 2.57±0.15 folds, respectively, as the cell volume was decreased by 22% ±11% and 35%±19% (Fig. 2E).

The cell volume reduction under osmotic compression was a result of cellular water efflux, which led to an increase in the concentration of intracellular materials (Guo et al., 2017). As a direct consequence, the effective stiffness of the cytoplasm was increased, as measured by optical tweezers (Hu et al., 2019) (Fig. 2C and Supplementary Fig. 1I, J), which were also positively correlated with TOP-Flash signals (Fig. 2F). Another consequence was the increased degree of molecular crowding as indicated by FRAP assay of Dendra II (Fig. 2D), which had been recognized to affect the biochemical reactions and biophysical processes (Akabayov et al., 2013; Ellis, 2001). These changes were resulted from an increased volume fraction of intracellular materials from 27.2±5.2% under isotonic condition to 38.4±8.4% under hypertonic condition (with 2% PEG 300), estimated by extracting all free water inside the cell with pure PEG 300 to obtain the minimal volume occupied by intracellular materials (Supplementary Fig. 1K–M). These results confirm that the degree of intracellular crowding increases as cell volume decreases under osmotic compression. Overall, the TOP-GFP signal is elevated as the cell volume decreases (Fig. 2G). These correlations were also observed when we replaced PEG with sucrose to compress RKO cells (Supplementary Fig. 1N–P) or increasing cell volume by other hypotonic media (Supplementary Fig. 1Q–S). Thus, we speculated that the molecular crowding serves as a physical regulator of Wnt/β-catenin signaling (Fig. 2H). Physical properties of cells also respond to other types of physical cues; for example, cell volume and intracellular crowding change as we vary substrate stiffness (Fig. 2I and Supplementary Fig. 2A and G), apply 3D mechanical compression (Fig. 2J, Supplementary Fig. 2B and I), or 2D isotropic stretch (Fig. 2K, Supplementary Fig. 2C and F). Consistently, we observed that Wnt signaling activity always traced the volume of cells, no matter how it was perturbed (Fig. 2I–K). Furthermore, when we blocked selective ion channels using NPPB or Gd^{3+} to suppress the volume change as substrate stiffness changes, the enhancement of Top flash signals was also significantly suppressed (Supplementary Fig. 2J). Additionally, actomyosin contractility can also regulate cell volume (Guo et al., 2017; Zhou et al., 2009). We found that inhibition of actomyosin contractility by blebbistatin increased cell volume, and resulted in a decrease in TOP-Flash signal; interestingly, application of additional osmotic compression to match the cell volume to the untreated cells rescued the decreased TOP-Flash signal (Supplementary Fig. 2K).

Molecular crowding enhances Wnt/β-catenin signaling by stabilizing cytosolic β-catenin upstream of the APC destruction complex

Wnt3a activates Wnt/β-catenin signaling through stabilization of β-catenin (Kim et al., 2013). By introducing hypertonic Wnt3a CM, we observed that an increased intracellular crowding markedly enhanced the TOP-Flash signals in both RKO cells and human embryonic kidney (HEK) 293T cells (Fig. 2L and Supplementary Fig. 3A). More than 80-fold increment over basal level signaling was observed in RKO cells with hypertonic Wnt3a-CM (Fig. 2L); this was nearly 3 times greater than the isotonic Wnt3a-CM. The qRT-PCR assay of Wnt target genes also showed elevated Wnt/β-catenin signaling, consistent with TOP-Flash reporter assay (Supplementary Fig. 3C). In contrast, hypertonic medium alone without Wnt3a, had no effect on Wnt/β-catenin signaling in RKO cells (Fig. 2L). Moreover, when endogenous Wnt secretion was blocked by IWP2 in HEK293T cells, the increase of Top-Flash signal under compression did not occur (Supplementary Fig. 3A). These suggest that intracellular crowding promotes Wnt/β-catenin signaling dependent of Wnt ligands.

Furthermore, Western blotting (WB) analyses also revealed a higher cytosolic β-catenin accumulation in a more crowded cytoplasm in both RKO and HEK293T cells (Fig. 2M and Supplementary Fig. 3B). This result is consistent with the decrease in both CK1-phosphorylated β-catenin and GSK3-phosphorylated β-catenin upon Wnt3a treatment within 30 mins (Supplementary Fig. 3D). In addition, no accumulation of cytosolic β-catenin was observed in RKO cells and IWP2 treated HEK293T cells with control medium (Fig. 2M and Supplementary Fig. 3D). This was further confirmed by fluorescent immunostaining of β-catenin (Fig. 2N), nearly doubling the amount under compression over isotonic Wnt3a-CM (Fig. 2N, O).

To test whether intracellular crowding directly impact β-catenin, we performed reporter assays in a human colorectal adenocarcinoma cell line, DLD1, which harbours adenomatous polyposis coli (APC) mutations resulting in elevated β-catenin accumulation (Fodde et al., 2001; Morin et al., 1997). Enhancement of neither TOP-Flash nor the β-catenin level was seen under compression (Fig. 2L, M). This suggests that intracellular crowding may work upstream of the APC destruction complex. To further validate this hypothesis, we overexpressed β-catenin and constitutively active β-catenin with mutations in S33, S37 and S41 in both RKO and HEK293T cells to activate Wnt signaling downstream of the receptor level (Supplementary Fig. 3E–H); no further enhancement was detected under compression, consistent with the observation in DLD1 cells, SW480 cells and Ls174T cells (Fig. 2L and Supplementary Fig. 3I, J). Moreover, Wnt signaling can be activated alternatively by overexpressing LRP6 (Zeng et al., 2005) or Dvl2 (Kishida et al., 2001); we found that compression with 2% PEG again induced a 2-fold enhancement of the TOP-Flash signal in RKO cells when either LRP6 or Dvl2 was overexpressed, as compared to those under isotonic condition (Supplementary Fig. 3K). These results suggest that compression effect may occur at the level of membrane receptor complex to impact Wnt/β-catenin signaling (Zeng et al., 2005).

Molecular crowding stabilizes the LRP6 signalosome

Upon Wnt3a stimulation, a receptor complex on the cell membrane is formed between Frizzled (Fz) and LRP6, resulting in phosphorylation and activation of LRP6 and its recruitment of Axin to the plasma membrane (Zeng et al., 2005). Wnt-induced clustering of the Fz-LRP6 complex with Axin and Dvl, referred to collectively as signalosome (Bienz, 2014; Gammons and Bienz, 2018; Gammons et al., 2016a; Gammons et al., 2016b; Johansson et al., 2019; Madrzak et al., 2015; Metcalfe et al., 2010; Tauriello et al., 2012; Valnohova et al., 2018), inhibits degradation of β-catenin, thereby leading to its stabilization and accumulation (Bilić et al., 2007; Metcalfe and Bienz, 2011). Indeed, we observed that compression increased Wnt3a-induced phosphorylation of LRP6 (Supplementary Fig. 3L–N), while the amount of Wnt3a ligand per cell did not change (Supplementary Fig. 4A, B). Significant enhancement of both cytosolic β-catenin accumulation and LRP6 phosphorylation was correlated with levels of intracellular crowding (Fig. 3A). This became more evident 30 min after Wnt3a treatment in comparison to cells without compression (Fig. 3A). Both the total accumulation of β-catenin and phosphorylation rate of LRP6 was higher when cells were compressed (Fig. 3B, C).

To further investigate whether the formation of LRP6 signalosomes was enhanced under compression, we co-transfected Axin1-mCherry (red signal) and LRP6-GFP (green signal) in RKO cells and monitored their co-localization using live cell imaging (Fig. 3D and Supplementary Movie 1). Without treatment of Wnt3a, Axin was localized either homogeneously in the cytoplasm or in intracellular puncta, while LRP6 was mainly distributed on the plasma membrane; no overlay was visualized (Supplementary Fig. 4C). However, within 15 min of Wnt3a treatment, a small fraction of LRP6 proteins started to coalesce into punctate structures at or below the plasma membrane, co-localizing with Axin1 (yellow dots) (Fig. 3D). Time-dependent measurements showed that these LRP6-Axin signalosomes formed faster under compression than isotonic condition, and the number of signalosomes plateaued in 40–45 minutes in both conditions. Both the number and intensity of LRP6-Axin signalosomes per cell increased with higher molecular crowding under compression (Fig. 3D, E). Additionally, we also simulated the enzyme kinetics of Axin-LRP6 binding versus total cellular Axin concentration. We transfected RKO cells with varied doses of Axin1, and quantified the total fluorescent intensity of the overall Axin and those formed signalosomes in each cell. This measurement can be well-fitted by an enzyme kinetics simulation of the following binding process: $nLRP6 + mAxin \underset{Koff}{\overset{Kon}{\rightleftharpoons}} nLRP6 \cdot mAxin$ with m=4 and n=3, indicating a constant equilibrium disassociation rate $K_D = K_{off}/K_{on}$. By stimulating these fluorescent data with or without osmotic compression, we showed a higher ratio of Axin-LRP6 binding and a 50% lower K_D as the degree of molecular crowding was increased (Supplementary Fig. 3O).

Co-immunoprecipitation (co-IP) of endogenous proteins also showed that the amount of Axin-associated LRP6 appeared to increase by 50% under a higher degree of molecular crowding after 2 hours of Wnt3a treatment (Fig. 3F), as well as Axin-associated Dvl2 and β-catenin (Supplementary Fig. 4K–M). Consistently, co-transfection of several complementary signalosome components confirmed that the formation of LRP6 signalosome was enhanced

in RKO cells under compression (Supplementary Fig. 4D–I). In addition, other mechanical loads that induce cell volume reduction, such as 2D stretching, also enhanced the signalosome formation (Supplementary Fig. 4S–U). Furthermore, using sucrose gradient assay, we observed that the molecular weight distribution of LRP6 shifts from smaller to larger weight under compression (Fig. 3G and Supplementary Fig. 4N–R), along with other signalosome components (Axin1, Dvl2 and β-catenin) (Supplementary Fig. 4P–R), supporting our conclusion that compression promotes signalosome formation. In addition, it appeared that there were slightly more intracellular signalosomes under compression (Fig. 3D), which are also important components of the Wnt/β-catenin signaling (Taelman et al., 2010; Vinyoles et al., 2014). We also replaced full-length (FL) LRP6 with either VSVG-LRP6m5 or VSVG-LRP6m10 respectively, that prevents binding of LRP6 and Axin; as a result, both Wnt ligand stimulation and osmotic compression did not induce LRP6 signalosome formation (Supplementary Fig. 4J). Similar results were observed when we replaced FL Axin with Flag-Axin△DIX, which prevents Axin head-to-tail self-interaction and its interaction with DVL (Fiedler et al., 2011; Kishida et al., 1999; Schwarz-Romond et al., 2007) (Supplementary Fig. 4J). These results indicate that intracellular crowding regulates Wnt activation mechanistically through promoting LRP6 signalosome formation.

It has been reported that mechanical perturbations and osmotic stress may lead to other responses of cells, such as activation of YAP signaling (Dupont et al., 2011), activation of MAP kinase (Volonté et al., 2001), release of membrane β-catenin from cadherin-catenin association (Benham-Pyle et al., 2015; Nelson and Nusse, 2004; Whitehead et al., 2008), inhibition of GSK3β downstream of integrin signaling (Dajani et al., 2001; Samuel et al., 2011) and tumorigenic phosphorylation of β-catenin (Fernandez-Sanchez et al., 2015). We found that the enhancement in canonical Wnt/β-catenin signaling upon the increased degree of intracellular crowding is independent of these cellular responses. For example, no obvious induction of TOP-Flash signal was observed in YAP activating RKO and HEK293T cells, either with or without compression, suggesting the compression-induced enhancement in Wnt/β-catenin signaling is independent of YAP signaling (Supplementary Fig. 5A–F). Furthermore, we found that inhibiting MAP kinases (p38, JNK, ERK, using SB202190, SP600125 and PD98059 respectively) did not affect cytosolic β-catenin accumulation; further increasing intracellular crowding with osmotic compression significantly increased cytosolic β-catenin accumulation and TOP-Flash signal (Supplementary Fig. 5G–I). These results suggest that the enhancement in Wnt/β-catenin signaling is independent of MAP kinases. Moreover, using RKO cells which lack cadherin, we excluded the involvement of cadherin-catenin association. Additionally, the Akt/GSK3β mediated regulation is mainly involved in tumorigenic β-catenin signaling (Fernandez-Sanchez et al., 2015; Samuel et al., 2011), but independent of canonical Wnt/β-catenin signaling, demonstrated using *in vivo* knock-in mice (McManus et al., 2005). Another concern is that whether the cell volume decrease leads to intrinsic changes in gene expression. Indeed, we found that the most significant consequence of compression is the elevation of Wnt target gene, rather than the intrinsic changes in universal gene expression showed by house-keeping genes from our WB and qRT-PCR data (Fig. 2M, 3A and Supplementary Fig. 1N, 1K, 3C).

Volumetric Compression elevates intracellular crowding, and influences fate of ISCs in intestinal organoids

Intestinal organoids resemble the epithelial tissue organization in the native gastrointestinal tract and is a promising model for studying organ development and pathogenesis (Sato et al., 2009). It is known that Wnt/β-catenin signaling is a master pathway for intestinal homeostasis, and our results showed a strong correlation between intracellular crowding and Wnt/β-catenin signaling (Fig. 1L, N). Thus, we explored the physiological functionalities of compression-induced crowding in intestinal organoids. To do so, we first used an *ex vivo* approach and assessed the ability of isolated crypts to form organoids in 3D cultures. Intriguingly, we found that isolated crypts were more likely to form ISC clusters and mini-intestines with higher intracellular crowding in hypertonic medium compared to those in control medium (Supplementary Fig. 6A–B). Strikingly, intestinal organoids formed under hypertonic condition exhibited a larger size than those in isotonic condition, even though the volume of individual cells was reduced under compression (Supplementary Fig. 6C). Under further subculture, the organoids in hypertonic medium partially transited to ISC spheroids, suggesting a naïve undifferentiated state and elevated stemness of ISCs (Supplementary Fig. 6D, E). Additionally, the organoids in hypertonic medium contained fewer but larger crypt domains, and were more cystic (less differentiated), as shown in Supplementary Fig. 6D–G.

Since the volume of individual cells shrank under osmotic compression, the increased organoid size was likely a result of increased cell number due to a higher cell proliferation rate. To test this, we stained for cell proliferation marker Ki67 and EdU, and indeed observed more proliferating cells in colonies under compression (Supplementary Fig. 6H–K). We also observed more ISCs within the colonies under compression shown by Lgr5 and Olfm4 (Van der Flier et al., 2009) (Supplementary Fig. 6L–O), indicating an elevated ISC self-renewal. A similar promotion effect was also observed when organoids were cultured under mechanical compression (Supplementary Fig. 6P–Y). Furthermore, the increased degree of intracellular crowding in organoids under both osmotic and mechanical compression was confirmed using FRAP assays (Fig. 4A and Supplementary Fig. 6Z).

Moreover, we confirmed these results in 2D intestinal enteroid monolayers. 2D enteroid was recently introduced as a scalable *ex vivo* system that recapitulates many of the features of 3D organoid (Thorne et al., 2018). Here, we further confirmed that 2D enteroids also recapitulated the physical properties of ISCs and differentiated cells, including elongated Lgr5+ cells, and larger and rounder Lgr5− cells (Supplementary Fig. 7A–F). A higher osmotic stress also yielded more cells undergoing proliferation per area as indicated by EdU and Ki67 (Supplementary Fig. 7G–J), which is consistent with our observation in 3D organoids.

We further asked whether the promotion effect of compression on organoid growth could be augmented during prolonged culturing. Organoids were cultured for one month (sub-cultured every 5 days) in conventional organoid medium with additional 1% PEG. Immunostaining and imaging were done on the 4th day of each passage. Indeed, the prolonged compression promoted the growth of organoids consistently (Fig. 4B–C). More interestingly, after culturing of several passages under compression, a large portion of organoids (~70%) transited into ISC sphere phenotype with a high purity of stem cells,

exhibiting a transparent and round morphology (Fig. 4D–F). The number of ISCs in each organoid accumulated over passages (Fig. 4G, H), as well as proliferating cells in organoids indicated by EdU and Ki67 (Fig. 4I–L).

Volumetric compression-increased intracellular crowding promotes intestinal stem cell self-renew via elevating Wnt/β-catenin signaling

In intestinal crypt, ISCs self-renew under a high level of Wnt/β-catenin signaling, and go through differentiation when Wnt/β-catenin signaling subsides. We indeed found a higher Wnt/β-catenin signaling in ISCs and organoid under compression as reflected by the higher expression level of the Wnt target gene Lgr5 (Barker et al., 2007) (Fig. 4G, H). Quantification of other Wnt/β-catenin target genes such as Axin2, Lgr5, Sox9, Rnf43 and Olfm4 using RT-PCR also confirmed the elevated Wnt/β-catenin signaling (Fig. 5A and Supplementary Fig. 7K). Moreover, we observed more cells accumulating more β-catenin under compression (Fig. 5B–E), further confirming that more cells maintain a higher Wnt/β-catenin signaling under compression per organoid (Fig. 5D). In cystic organoids formed by ISCs with the *APC* gene depleted by lentiviral delivery of a short hairpin RNA, where Wnt/β-catenin signaling is always hyper-activated, compression affected neither growth nor Lgr5 expression (Fig. 5F–H). Meanwhile, inhibition of Porcupine (endogenous Wnt ligand production) using 1 μM IWP2, which blocks endogenous Wnt ligand secretion and therefore prevents signaling upstream of complex formation, supressed the growth of intestinal organoids; in this case, increasing intracellular crowding using osmotic compression did not rescue organoid growth (Fig. 5I). As a comparison, IWP2 treatment did not affect the growth of cystic organoids with *APC* depletion (Fig. 5I). Alternatively, we deleted endogenous *Wls* (a carrier protein transporting lipid-modified Wnts to the cell surface) (Bänziger et al., 2006; Bartscherer et al., 2006; Coombs et al., 2010; Yu et al., 2014)) in organoids using conditional shWLS. The complete depletion of endogenous *Wls* impair Wnt secretion upstream of complex formation and thus stops the growth of intestinal organoids (Fig. 5J); this is consistent with previous studies showing that organoids derived from *Villin-WLS*^{cKO} mice die without addition of external Wnts (Degirmenci et al., 2018; Valenta et al., 2016). In this case, increasing intracellular crowding using osmotic stress did not rescue organoid growth (Fig. 5J). As a comparison, complete depletion of *WLS* using shWLS did not affect the growth of cystic organoids with *APC* depletion (Fig. 5J). These results confirmed that compression promotes the growth of intestinal organoids through regulating Wnt/β-catenin signaling upstream of *APC* the destruction complex, likely at the LRP6 receptor level.

To confirm the elevated LRP6 signalosome formation induced by volumetric compression, we conducted signalosome formation assays in 2D intestinal enteroids. Indeed, the osmotic compression increased the phosphorylation of LRP6 in enteroid monolayer (Fig. 6D). Furthermore, we co-transfected Axin1-mCherry and LRP6-GFP in enteroid monolayer, and monitored their co-localization (Fig. 6B). The measurements were performed in “crypt-like foci” proliferative zones (Thorne et al., 2018) of 2D enteroids. The average number of signalosomes per cell in enteroids was elevated after osmotic compression (Fig. 6C). We also confirmed that osmotic compression increased the cytoplasmic stiffness of enteroid monolayers and reduced the diffusion rate of cytoplasmic Axin-mCherry (Fig. 6A, E), which suggested an increased the degree of cytoplasmic crowding. In addition, we used the FRAP

assay to characterize the Axin dynamics in signalosomes formed in 2D enteroid monolayers. We photo-bleached selected signalosomes and monitored the recovery of mCherry intensity. We observed the recovery of the bleached signalosome (Fig. 6F), which supported that the Axin inside and outside signalosome are exchanged dynamically over time. Without osmotic compression, the recovery $t_{1/2}$ of Axin in signalosomes was measured to be 23.6±4.0 s, which was increased to 30.0±5.8 s with compression (Fig. 6E). This result suggested a slower exchange of Axin between inside and outside of a signalosome under compression, consistent with the increased intracellular crowdedness. This result also confirmed that the signalosome is more stable in enteroid monolayers upon osmotic compression. Taken the results in 3D organoid and 2D enteroid together, we concluded that compression promoted the intestinal stem cell self-renewal and thus the enteroid/organoid growth via stabilizing the formation of LRP6 signalosome.

CONCLUSION

Efforts in recent years to understand the physical nature of the cell cytoplasm has gained increasing attention (Guo et al., 2014; Guo et al., 2017; Lee et al., 2014; Oakes et al., 2014). Here, our observations reveal a direct relationship between cellular physical property and cell fate decision, potentially contributing to organ homeostasis and development. We report that the compression-induced intracellular crowding in mammalian cells regulates a specific intracellular signaling pathway, i.e., canonical Wnt/β-catenin signaling, via modulating the LRP6 signalosome (Fig. 7). Our results provide insights into the interplay between physical properties of cells and biochemical signaling cascades: The activity of Wnt/β-catenin signaling tracks the degree of intracellular molecular crowding as perturbed by various types of extracellular physical cues (e.g.: volumetric compression, substrate stiffness and 2D stretch). Indeed, in intestinal crypts, not only proximity to Wnt ligand masters cellular Wnt/β-catenin signaling, the cellular physical properties (e.g.: volume) cooperatively modulate Wnt/β-catenin response dependent of Wnt ligand exposure.

We believe the impact of intracellular crowding on biochemical reaction rates and equilibrium in cells is a general effect, not only limited to those along the canonical Wnt/β-catenin signaling pathway. Nevertheless, whether this effect is significant enough to promote a particular signaling activity depends on the nature of its regulatory network, the level of the stress, and initial concentrations of corresponding proteins, which determines the specificity of the effected signaling pathways. For example, it has been recently shown that osmotic stress (generated by a minimum of 5% PEG) activated YAP target genes in cells (Cai et al., 2019). Our proposed model highlights the physical property of cells as a regulator of cellular functionality, which we believed is complementary to the current mechanobiology studies focusing on revealing mechanosensor. Future work could explore upstream mechanosensor in regulation of cell volume, which will further integrate our physical perspective of mechanoregulation with the classical studies of molecular mechanosensor.

On the physiological level, we identified distinguishing physical properties of $Lgr5^+$ ISCs, and showed that the properties correlate with Wnt/β-catenin signaling and Lgr5 expression. Reducing the cell volume with physical perturbations led to higher Wnt/β-catenin signaling

and self-renewing of ISCs. The insight of molecular crowding as a physical regulator in intestinal homeostasis and organoid growth provides an entry point for understanding the crucial but elusive physical cues in the stem cell niche and tissue homeostasis beyond the intestine: for example, the daily diet and digest can vary osmolarity in digestive tract microenvironment (Overduin et al., 2014); the expansion of tumors can significantly increase local physical stress in many tissues (Gutmann et al., 1992; Heldin et al., 2004; Netti et al., 1995). Finally, we demonstrated an application to engineer intestinal organoids and ISC colonies by manipulating the cellular physical properties via osmotic and mechanical compressions. Together with a recent study reported that high matrix stiffness significantly enhances ISC sphere expansion through a YAP-dependent mechanism (Gjorevski, 2016), we anticipate many physical regulators and engineering approaches of different types of organoids to be revealed in the coming years.

Limitations of Study

Despite the Wnt/β-catenin signaling is the master signaling pathway in intestinal organoid development, there are still many other pathways involved to fine tune the cell fate in organoid growth. This study does not include what contributions the intracellular crowding has made to other cellular signaling pathways and further cell lineage commitments beyond the first differentiation of ISCs. In this study, we mainly used mouse intestinal epithelium and organoids, and it will be important to extend these phenotypic findings to human resourced tissues. Additionally, the Wnt/β-catenin signaling is involved in other tissues, including lung and liver, suggesting that study of intracellular crowding on other living tissues and organoids may provide more comprehensive understandings of cellular physical properties in developments.

STAR⋆ METHODS

RESOURCE AVAILABILITY

Lead Contact—Further information and requests for resources and reagents should be directed to and will be fulfilled by the Lead Contact, Ming Guo (guom@mit.edu).

Materials Availability—This study did not generate new unique reagents.

Data and Code Availability—This study did not generate datasets. MATLAB scripts used in this work are available from the Lead Contact upon reasonable request.

EXPERIMENTAL MODEL AND SUBJECT DETAILS

Cell lines—RKO cells (ATCC® CRL-2577™), HEK293T cells (ATCC® CRL-11268), SW480 cells (ATCC® CCL-228™), LS 174T cells (ATCC® CL-188™), DLD-1 (ATCC® CCL-221™), Mouse L cells (ATCC® CRL-2648™) and L Wnt3A cells (ATCC® CRL-2647™) were obtained from ATCC with a certificate of authentication with STR profiling. Cell lines were confirmed to be mycoplasma-negative when cultures were started in the lab. All cell lines were cultured using DMEM medium supplemented with 10% Fetal Bovine Serum (FBS) at 37°C with humidified atmosphere of 5% CO2. Mouse L cells

(ATCC® CRL-2648™) and L Wnt3A cells (ATCC® CRL-2647™) were used for preparation of control and Wnt3A conditioned medium according to ATCC protocol.

Mice—Intestinal crypts were extracted from 3–5 week old wild type C57BL6/J or heterozygous Lgr5-eGFP-IRES-CreERT2 (Jackson Laboratory) and Olfm4-IRES-eGFPCreERT21 mice (Van der Flier et al., 2009). Olfm4-IRES-eGFPCreERT21 mice were imported from Clevers laboratory. Subjects were not involved in previous procedures, and they were drug and test naive. Mice were quarantined at Jackson Laboratory to make sure they were healthy and free of infectious agents. Animals had free access to food and water throughout the study. All mouse experiments were approved by Boston Children's Hospital (BCH) Institutional Animal Care and Use Committee (IACUC) and performed under protocol 15–01-2869R. Animals were housed and handled in accordance with protocols approved by Animal Research at Boston Children Hospital's Hospital (ARCH).

METHOD DETAILS

Intestinal crypt isolation—Murine intestinal crypts were isolated following the protocol described previously (Sato et al., 2009). Briefly, the proximal part of the intestines was isolated, opened longitudinally and washed with ice-cold PBS. The intestinal tissue was chopped into 2 to 4 mm pieces, and washed by ice-cold PBS. Crypts were released by incubating intestinal pieces in ice-cold 2mM EDTA. The chopped samples were centrifuged and re-suspended for several times. The supernatant was further collected and passed through a 70-μm strainer for crypt enrichment. All the collected crypts were combined and centrifuged at 200 g for 5 min to remove single cells and tissue debris. The enriched crypts were embedded in Matrigel (BD Biosciences; growth factor reduced, phenol redfree formulation). To passage the crypts, the colonies were enzymatically dissociated by treating with 1 mL TrypLE Express (Life Technologies) for 5 min at 37 °C.

Uniaxial stretching of intestine—To apply a 2D uniaxial stretching of intestine, the proximal part of mouse intestines was isolated, washed with ice-cold PBS and chopped into 1 cm pieces. An individual intestine piece (1 cm by 1 cm) was glued on two polystyrene clamps on two ends, and stretched at room temperature on a confocal microscope. Both loading and unloading rates were kept constant at 5 mm per minute. We held the two clamps when the total length of the intestine piece reached 1.7 cm, corresponding to 70% engineering strain of the bulk intestine piece. 3D confocal imaging was then performed at the center area of the intestine piece.

Inhibition and blocking of ion channels and aquaporin-channels—To block ion channels, 0.1 mM 5-nitro-2-(3-phenylpropylamino)-benzoic acid (NPPB) was added to the medium to inhibit chloride ion channels after cells fully spread. Meanwhile, 10μM gadolinium (iii) chloride was added into the medium to use as a wide spectrum blocker of mechanosensitive ion channels. To block aquarin-channels, cells were treated with 100 mM TGN-020 for blocking aquaporin 4. All the experiments were carried out after 1 hour of treatment with these blockers.

Intestinal stem cell (ISC) and organoid culture—Freshly isolated mouse crypts or single cells from dissociated mouse ISC colonies were embedded in Matrigel, which were cast into 50 μL droplets at the bottom of wells in 24-well plate. After gelling at 37 °C for 5 to 10 min, the gels were overlaid with 500 μL of ISC expansion medium (Advanced DMEM/F12 containing Glutamax, HEPES, penicillin-streptomycin, B27, N2 (Invitrogen) and 1 μM N-acetylcysteine (Sigma)), supplemented with growth factors, including EGF (50 ng mL^{-1}; Peprotech), Noggin, Wnt3a and R-spondin (conditioned medium from mouse L-WRN cell line (Miyoshi and Stappenbeck, 2013)). To induce organoid formation and differentiation, the ISC expansion medium was replaced with fresh organoid medium containing EGF (Peprotech), Noggin (Peprotech) and R-spondin (conditioned medium from HEK293T stably expression R-spondin 1).

2D Intestinal enteroid monolayers culture—Freshly isolated mouse crypts were pelleted at 150 × g for 3 mins and suspended in 2D attachment media (advanced DMEM/F12 media supplemented with EGF (50 ng/ml, Invitrogen #PMG8043), LDN-193189 (100 nM, Sigma-Aldrich #P4543), R-spondin 1 (1 mg/ml, R&D Biosystems #3474-RS-050), CHIR99021 (10 mM, Selleck #S1263), Y-27632 (10 mM, Selleck #S1049), 1x N-2 supplement (Invitrogen #17502–048), 1x B-27 supplement (Invitrogen #17504–044), 10mM HEPES (Invitrogen #15630–080), 1x Glutamax (Invitrogen #35050–061), 1mM N-acetyl-cysteine (Sigma-Aldrich #A9165), 1x penicillin, and 1x streptomycin)). The concentration of isolated crypts was estimated using a hemocytometer.

Prior to seed 2D crypt, 96-well plates were first coated with growth factor reduced Matrigel (Corning #356231). Practically, 96-well plates were incubated with 50 μL of 0.8 mg/mL Matrigel diluted in organoid medium at 37 °C for one hour, which allows Matrigel to polymerize and coat the bottom of the well. 50–100 crypts were then seeded into each well of the 96-well plate and incubated in the attachment medium for 4 hours. The cells were then wash with media to remove unattached cells and replaced in organoid media for further culturing. To stimulate 2D enteroid monolayers with osmotic compression, 1% PEG (V/V) was added into organoid media to generate osmotic stress.

Luciferase reporter assays (TOP-Flash assay and 8xGTIIC assay)—Mammalian cell transfections were done in HEK293T cells and RKO cells using FuGENE 6 and performed in triplicate. The cells were plated at 1×10^5/mL in 24-well plates and transfected the following day with a total of 0.4 μg of DNA/well (0.1 μg of TOPFLASH/8xGTIIC assay, 0.01 μg of thymidine kinase promoter Renilla, 0.09 μg of pCS2 (empty vector), and up to 0.2 μg of experimental DNA constructs). The lysates were collected 48 h post-transfection and used with the dual luciferase reporter system (Promega). Firefly and Renilla luciferase activity was measured using the Wallac 1420 multilabel counter in 96-well plates. The Firefly signal was firstly normalized to Renilla signal. Normalized data expressed in relative luciferase units was averaged from triplicate assays, and the error bars reflect the standard deviations.

Fluorescence recovery after photo-bleaching (FRAP)—FRAP experiments on Dendra II in live cells were performed at 37 °C and 5% CO_2 in a live cell chamber mounted on a Leica SP8 confocal microscope with a 63x (NA 1.3) water objective. Photo-bleaching

of Dendra II was achieved using a 488 nm laser with a bleaching time of 865 ms. Images (512 X 512 pixels, 8 bit depth) were captured at 173 ms internals with a scanning speed of 1000 Hz for 100 time points. As a reference, another spot with uniform fluorescence Dendra II signal not exposed to laser-bleaching was also recorded. The measured FRAP data was firstly normalized to the reference signal to eliminate the possible imaging associated photo-bleaching effect during data acquisition. The normalized data was fitted with a single exponential recovery curve. The time it takes for the fluorescence to recover to 50% of the asymptote (plateau) intensity is defined as recovery half-time, $t_{1/2}$, which is calculated from the fitting curve. The recovery half-time $t_{1/2}$ indicates the apparent diffusion rate of Dendra II, which was used as a parameter in this study to indicate the degree of intracellular crowding.

Immunofluorescence analysis of ISC and intestinal organoid—ISC spheroids or organoids cultured under different conditions in Matrigel were fixed with 4% paraformaldehyde (PFA) in PBS for 30 min at room temperature. The fixation process led to full degradation of the Matrigel. Suspended colonies were collected and centrifuged at 800 rpm for 5 min to remove PFA. The pellets were washed with ultrapure water. The ISCs and organoids were re-suspended in water. The ISCs were pipetted onto glass slides and allowed to attach by drying. Attached colonies and organoids were rehydrated with PBS. Then, the organoids spread on glass were permeabilized with 0.2% Triton X-100 in PBS for 1 hour and blocked with 3% BSA in PBS containing 0.01% Triton X-100 for 3 hours. Samples were incubated with primary antibodies (anti-Ki67, 1:50, 9129S, Cell Signaling Technology; anti-β-catenin, 1:50, 8480S, Cell Signaling Technology). After rinsing with PBS for at least 3 hours, colonies were incubated overnight at 4 °C with secondary antibody Alexa 488 goat-anti-rabbit (1:1000, Invitrogen) in block solution. After incubation, the residual antibodies were removed by rinsing with PBS for at least 3 hours. Finally, the stained ISCs and organoids were imaged with confocal microscopy (Leica SP8).

EdU cell proliferation assay and quantification—ISCs and organoids were incubated with EdU for 2 hours before fixation and imaging. After incubation with EdU, the colonies were fixed with PFA in suspension, and further attached to glass coverslips as described above. The colonies were rehydrated by pure water. Following washing the cells with 3% BSA in PBS, the colonies were penetrated using 0.5% Triton X-100 in PBS for 1 hour at room temperature. To perform EdU staining, cells were treated with Click-iT® Plus reaction cocktail (Invitrogen™) for 30 min according to the manufacturer's instruction. Finally, the residual reaction cocktail was removed and further washed with 3% BSA in PBS. Prior to imaging, the samples were stained with DAPI for nuclear staining. The staining of EdU was quantified by the ratio of cells positive with EdU staining.

Immunoblotting, Immunoprecipitation, and immunofluorescence—Cell lysates were prepared in RIPA buffer (with a cocktail of phosphatase and protease inhibitors (Roche)) for total protein extraction. For preparation of cytosolic proteins, cells were lysed with 0.015% digitonin in PBS containing a cocktail of protease inhibitors and phosphatase inhibitors (Roche). For immunoprecipitations, cell lysates from HEK293T or RKO cells were incubated with the primary antibody for 2–4 hours at 4 °C, followed by incubated with

50% slurry of protein G-sepharose and overnight incubation at 4 °C. Precipitates were washed with lysis buffer 5 times and boiled with 2 × SDS sample buffer before loading for SDS-PAGE. For quantification of immunoblotting, the gray scale intensity of blotted bind was analyzed and obtained using software ImageJ after subtracting the background. The relative intensity of target proteins was normalized to blotted house-keeping protein GAPDH. For quantification of immunoprecipitation, the gray scale intensity of co-precipitated protein was normalized to the gray scale intensity of either input or binding pair protein.

For immunofluorescence, cells were then fixed with 4% paraformaldehyde for 30 min at room temperature, and then penetrated by 0.2% tritton-X100 for 1 hour and incubated with primary antibodies overnight. After careful removal of primary antibodies by rinsing with PBS, cells were treated with secondary antibodies for 4 hours at room temperature. Following extensive washing, stained cells were imaged with confocal microscopy (Leica SP8). The quantifications of immunofluorescence were performed either using the ratio of the positively stained cells or using relative fluorescence intensity per cell. Prior to image analysis, the background fluorescent intensity was subtracted from the acquired images. Cell segmentations were performed using TrackMate plugin function in software ImageJ. The relative signals of certain proteins in each cells were calculated by summing up the fluorescent intensity in the area of segmented individual cells. For colocalization analysis in signalosome formation experiments, a mask was generated based on the LRP6 staining image. We only quantify the cells expressing normal amount of transfected protein. This mask was further applied to other components (Axin, FZD, Dvl) staining images. The number of Axin/FZD/Dvl particles was counted from the masked Axin image using TrackMate plugin-in function of ImageJ. The counted numbers were averaged per cells to quantify the formed signalosome in each conditions.

Quantification of ISC/organoid colony formation, ISC/organoid size and morphology—To quantify the colony formation efficiency of embedded ISCs and organoids, z-stacks of the whole Matrigel sample across the entire thickness were taken by confocal microscopy to quantify the fraction of cells that formed colonies, at day 0 and at day 4 after seeding. To measure colony size, the roundness index and the larger diameter of each colony was measured in ImageJ. The roundness index is defined by: $4\times Area/(\pi\times MajorAxis^2)$.

Lantivirus production and transduction—Lentiviral particles expressing shRNA targeting APC or a non-targeting control shRNA were generated in HEK293T cells by co-transfection of the shRNA plasmids with the third generation lentivirus packaging vectors. 48 hours after transfection, the supernatant was collected, filtered and ultra-centrifuged at 50,000 g for 2 hours at 4 °C. The pellet was collected and re-suspended in ISC medium. Lentiviral infection of ISCs was carried out by firstly dissociating the ISC spheres. The cells were re-suspended in the infection medium (Virus containing medium + Y-27632 + polybrene) and transferred to a 24-well plate. The plate was centrifuged 1 hour at 600g (spinoculation) and incubated for 6 hours in a tissue culture incubator. The infected ISCs were then collected for recovery and colony formation.

Fabrication of polyacrylamide gel substrate—Polyacrylamide gels with various stiffnesses were fabricated on a 35 mm glass-bottom culture dish (MatTek, Ashland, MA) according to the procedure previously described (Pelham and Wang, 1997). Briefly, the bottom No.1 coverslip was aminosilanized to enable polyacrylamide attachment. Gel stiffness was varied by adjusting the concentrations of the monomer acrylamide (Bio-Rad) and the cross-linker bis-acrylamide (Bio-Rad, Hercules, CA). Gels with a shear modulus of 7 kPa were made of 7.5% acrylamide and 0.1% bis-acrylamide, while those of 200 Pa were made of 3% acrylamide and 0.08% bis-acrylamide. The polymerization was initiated by the addition of ammonium persulfate and n,n,n',n'-tetramethylethylenediamine (TEMED). Immediately after initiating polymerization, a controlled volume was added to the glass bottom dishes. Then, another unmodified coverslip was placed on top to cover the polymerizing gel to ensure a flat gel surface. After fully polymerized, we removed the top coverslip and functionized the gel surface with collagen I (0.1 mg/mL; Invitrogen; Cohesion Tech, Palo Alto, CA) using sulfo-SANPAH (Pierce Biotechnology, Rockford, IL) activation method (Wang and Pelham, 1998). Collagen attachment and uniformity were confirmed using fluorescent collagen (Elastin Products, Owensville, MO). The thickness of gel was controlled to be 70–100 μm and confirmed by confocal microscopy. The polyacrylamide gel is a linear elastic material at small deformation, and the shear modulus G' of macroscopic samples was measured using a rheometer (AR-G2; TA Instruments, New Castle, DE).

3D volume measurement—Cells in 2D culture for volume measurement were stained with CellTracker™ Green CMFDA Dye (Invitrogen™). Cells in crypt, enteroid monolayers and organoids for volume measurement were stained with anti-E-cadherin. Volume is calculated based on cell tracker to see the body, and E-cadherin to see the boundary, which allow us to calculate the volume precisely. 3D cell images were obtained using 63x/1.2NA water immersion lens on a confocal microscope (Leica SP8, Germany). Cells that we imaged were randomly picked. The optical cross-sections were recorded at 0.15 micron z-axis intervals to show intracellular, nuclear, and cortical fluorescence. x-y pixel size was chosen to be comparable to z-axis interval to achieve better voxel resolution and better deconvolution results. The 3D image was deconvolved using a Huygens Software before 3D visualization. 3D visualization was carried out using ImageJ, AMIRA software and LAS X 3D Visualization from Leica. The volume of cells and cell nuclei were calculated by counting voxel number, after thresholding the stack using a home-built Matlab algorithm. The threshold was selected as the fluorescent intensity on the bottom interface of the cells which could be identified from the confocal reflection imaging. The confocal measurement of cell volume had been previously compared with measurement using atomic force microscopy (AFM) and super resolution structured illustration microscopy, showing consistent results for both the cell height and cell volume (Zhou et al., 2009).

Osmotic stress—Hyperosmotic stress was applied by adding polyethylene glycol 300 (PEG300) to isotonic culture medium. The correlation between molarity and osmolality for solutions of PEG in water was taken from previous measurement (http://www.brocku.ca/researchers/peter_rand/osmotic/osfile.html). The actual osmotic pressure applied to cells was calculated by summing up the osmotic pressures of PEG and isotonic medium (325 mOsm), and was further validated by measurement using a micro-osmometer (model 3300,

Advanced Instruments, Inc.). Cells were incubated for 10 min at 37 °C and 5% CO_2 for equilibrate in PEG solution. The cell size and mechanics achieved equilibration within 2 minutes after adding PEG 300 based on previous studies(Guo et al., 2017; Zhou et al., 2009). The hypotonic medium was prepared by diluting DMEM medium in distilled water, which was also recovered to isotonic medium with additional PEG300 to match the osmolality of pure DMEM medium. Alternatively, we also generated hyperosmotic stress by adding different amounts of sucrose to isotonic culture medium.

Optical tweezers setup and calibration—The beam from a variable-power solid-state laser (5 W, 1064 nm) was employed to optically trap and manipulate micron-size beads in the cytoplasm of living cells. The beam was steered through a series of Keplerian beam expanders to overfill the back aperture of a 100× 1.3 numerical aperture trapping objective (Leica, Germany). For detection, the bead was centered on a high–resolution position detection quadrant detector (Thorlabs, US). The linear region of the detector was calibrated by trapping a bead identical to those used in the cells in a 41% sucrose solution that was refractive index matched with the cell(Hu et al., 2017; Jun et al., 2014) and moving it across the detector using an acousto-optic deflectors in known step sizes; a trap stiffness was determined as 0.05 pN/nm. Beads displacement was maintained in the linear region. A trapped bead was dragged across at a speed of 1 μm/s using a high-resolution XYZ piezo stage.

Mechanical compression of cells cultured in 3D Matrigel—To mechanically compress cells in 3D culture, RKO cells were encapsulated in Matrigel sandwiched by two porous membranes. A weight was placed on the top membrane to introduce a vertical compression. We induced two levels of stresses (σ), 76 Pa and 173 Pa respectively. As the area of the sample was confined by the glass slides, the gel only deformed in z direction under vertical compression. Upon stress, the sample firstly deformed poroelastically, and eventually achieved an equilibrate deformed state. The relative vertical deformations of the Matrigel were measured using confocal reflection microscopy to be ~20% and ~45%, which were consistent with the estimated engineering strain (σ/E), 18% and 40%, respectively, calculated using an elastic modulus of Matrigel E~450 Pa (Soofi et al., 2009). Consistently, a decrease of the volume of embedded cells (20% and 44% reduction, respectively) was observed under the two levels of mechanical compression.

Stretching the cells using a PDMS elastomer bottom device—To stretch cells mechanically, we developed a PDMS elastomer-based cell stretching device in a petri-dish, which consisted of a PDMS sheet bottom with a ring-shape insert for applying static isotropic biaxial stretch. RKO cells were uniformly seeded on the PDMS membrane, which was then isotropically stretched. We observed a relative deformation ~20% in the diameter of cells. After stretching, both the cell volume and the diffusion of intracellular fluorescent proteins were measured to confirm the change in the degree of intracellular molecular crowding. We then maintained the isotropic stretch overnight, and after overnight incubation, cells were harvested and the lysates were used for TOP-Flash assay.

Enzyme kinetics simulation—For the enzyme kinetics simulation, we consider the following binding process:

$$nLRP6 + mAxin \underset{Koff}{\overset{Kon}{\rightleftharpoons}} nLRP6 \cdot mAxin$$

As initial conditions, the ratio of the *Axin* concentration (*[Axin]*) and LRP6 concentration (*[LRP6]*) varies from 1 to 100, which represents the increase of *[Axin]* due to either osmotic pressure or transfection. We then simulate the change of *[Axin]*, *[LRP6]* and *[nLRP6mAxin]* with time until the binding reached equilibrium and all concentrations remain steady. The binding rate is $K_{on}[Axin]^m[LRP6]^n$, and the dissociation rate of the signalosome is $K_{off}[nLRP6mAxin]$ in the simulation. We find the measurement under different transfection level can be well-fitted with $n=3$, $m=4$ and $K_D=3$, where $K_D = K_{off}/K_{on}$ is the dissociation constant, an important equilibrium constant for a chemical reaction. With $n=3$, $m=4$ and $K_D=1.5$, the simulation result fits the measurement under high osmotic pressures well, which shows a significant decrease of K_D with the increase of osmotic pressure.

Sucrose gradient sedimentation and coimmunoprecipitation—About 20 hours post transfection, HEK 293T cells were treated for 3 hours with control medium, Wnt3a conditioned medium and hypertonic Wnt3a conditioned medium, respectively. Cells were harvested in Hank's Balanced Salt Buffer on ice, pelleted, and lysed for 20 min in extraction buffer: 30 mM Tris (pH 7.3), 140 mM sodium chloride, 1% Triton X-100 (Sigma), 25 mM sodium fluoride, 3mM sodium ortho-vanadate, 2 mM PMSF, 100 nM okadaic acid and protease inhibitor cocktail tablete (Roche). Lysates were centrifuged, and supernatant was layered on top of a 15–40% sucrose gradient in 30 mM Tris (pH 7.3), 140 mM sodium chloride, 0.02% Triton X-100, 25 mM sodium fluoride, 3mM sodium ortho-vanadate and protease inhibitors. Ultracentrifugation was done in a Beckman SW60 rotor at 43.000 rpm, 4 hours, 4°C. After centrifugation, sucrose was diluted by adding 400 µl extraction buffer to 800 µl sample, and incubated for 4 h with FLAG M2 beads (Sigma) at 4°C. After washing with extraction buffer, proteins were eluted with loading buffer at 50°C for 10 min, following western blot analysis.

QUANTIFICATION AND STATISTICAL ANALYSIS

Statistically significant differences between the means of two groups were assessed using a Student's t-test, whereas data containing more than two experimental groups were analyzed with a one-way analysis of variance followed by a Bonferroni's multiple comparison test. In the experiment of Sucrose gradient assay, the statistically significant differences are evaluated using multivariate analysis of variance (MANOVA). Err bars in all figures represent standard deviation. All statistical analyses were performed in the Origin 9.0 software. *p<0.05, **p<0.01, ***p<0.001, respectively.

Supplementary Material

Refer to Web version on PubMed Central for supplementary material.

ACKNOWLEDGEMENTS

The authors would like to acknowledge the support from National Cancer Institute grant no. 1U01CA202123 and the Jeptha H. and Emily V. Wade Award at MIT. M.G. acknowledges the Sloan Research Fellowship. X.H. acknowledges support by NIH (RO1-GM057603 and RO1-GM126120), and by Boston Children's Hospital Intellectual and Developmental Disabilities Research Center (NIH P30 HD-18655), and by the Harvard Digestive Diseases Center (NIH P30DK034854). X.H. is an American Cancer Society Research Professor. The authors thank Dr. Ibrahim Cissé for DendraII plasmid, and Drs. Hans Clevers and Alan Hanash for Olfm4-IRES-eGFPCreERT2 mice, and Dr. T. Stappenbeck for mouse L-WRN cell line.

REFERENCES

Akabayov B, Akabayov SR, Lee S-J, Wagner G, and Richardson CC (2013). Impact of macromolecular crowding on DNA replication. Nature communications 4, 1615.

Bänziger C, Soldini D, Schütt C, Zipperlen P, Hausmann G, and Basler K (2006). Wntless, a conserved membrane protein dedicated to the secretion of Wnt proteins from signaling cells. Cell 125, 509–522. [PubMed: 16678095]

Barker N, and Clevers H Tracking Down the Stem Cells of the Intestine: Strategies to Identify Adult Stem Cells. 133, 1755–1760.

Barker N, van Es JH, Kuipers J, Kujala P, van den Born M, Cozijnsen M, Haegebarth A, Korving J, Begthel H, and Peters PJ Identification of stem cells in small intestine and colon by marker gene Lgr5. Nature 449, 1003–1007.

Barker N, Van Es JH, Kuipers J, Kujala P, Van Den Born M, Cozijnsen M, Haegebarth A, Korving J, Begthel H, and Peters PJ (2007). Identification of stem cells in small intestine and colon by marker gene Lgr5. Nature 449, 1003–1007. [PubMed: 17934449]

Bartscherer K, Pelte N, Ingelfinger D, and Boutros M (2006). Secretion of Wnt ligands requires Evi, a conserved transmembrane protein. Cell 125, 523–533. [PubMed: 16678096]

Batlle E, Henderson JT, Beghtel H, van den Born MM, Sancho E, Huls G, Meeldijk J, Robertson J, van de Wetering M, and Pawson T (2002). B-Catenin and TCF mediate cell positioning in the intestinal epithelium by controlling the expression of EphB/ephrinB. Cell 111, 251–263. [PubMed: 12408869]

Benham-Pyle BW, Pruitt BL, and Nelson WJ (2015). Mechanical strain induces E-cadherin–dependent Yap1 and β-catenin activation to drive cell cycle entry. Science 348, 1024–1027. [PubMed: 26023140]

Biechele TL, and Moon RT (2008). Assaying β-catenin/TCF transcription with β-catenin/TCF transcription-based reporter constructs In Wnt Signaling (Springer), pp. 99–110.

Bienz M (2014). Signalosome assembly by domains undergoing dynamic head-to-tail polymerization. Trends in biochemical sciences 39, 487–495. [PubMed: 25239056]

Bilić J, Huang Y-L, Davidson G, Zimmermann T, Cruciat C-M, Bienz M, and Niehrs C (2007). Wnt induces LRP6 signalosomes and promotes dishevelled-dependent LRP6 phosphorylation. Science 316, 1619–1622. [PubMed: 17569865]

Bursac P, Lenormand G, Fabry B, Oliver M, Weitz DA, Viasnoff V, Butler JP, and Fredberg JJ (2005). Cytoskeletal remodelling and slow dynamics in the living cell. Nature materials 4, 557. [PubMed: 15937489]

Cai D, Feliciano D, Dong P, Flores E, Gruebele M, Porat-Shliom N, Sukenik S, Liu Z, and Lippincott-Schwartz J (2019). Phase separation of YAP reorganizes genome topology for long-term YAP target gene expression. Nature cell biology 21, 1578–1589. [PubMed: 31792379]

Cheng H, and Leblond CP (1974). Origin, differentiation and renewal of the four main epithelial cell types in the mouse small intestine. III. Entero endocrine cells. American Journal of Anatomy 141, 503–519.

Chowdhury F, Na S, Li D, Poh Y-C, Tanaka TS, Wang F, and Wang N (2010). Material properties of the cell dictate stress-induced spreading and differentiation in embryonic stem cells. Nature materials 9, 82. [PubMed: 19838182]

Coombs GS, Yu J, Canning CA, Veltri CA, Covey TM, Cheong JK, Utomo V, Banerjee N, Zhang ZH, and Jadulco RC (2010). WLS-dependent secretion of WNT3A requires Ser209 acylation and vacuolar acidification. Journal of cell science 123, 3357–3367. [PubMed: 20826466]

Crowder SW, Leonardo V, Whittaker T, Papathanasiou P, and Stevens MM (2016). Material cues as potent regulators of epigenetics and stem cell function. Cell stem cell 18, 39–52. [PubMed: 26748755]

Dajani R, Fraser E, Roe SM, Young N, Good V, Dale TC, and Pearl LH (2001). Crystal structure of glycogen synthase kinase 3β: structural basis for phosphate-primed substrate specificity and autoinhibition. Cell 105, 721–732. [PubMed: 11440715]

Degirmenci B, Valenta T, Dimitrieva S, Hausmann G, and Basler K (2018). GLI1-expressing mesenchymal cells form the essential Wnt-secreting niche for colon stem cells. Nature 558, 449–453. [PubMed: 29875413]

Delarue M, Brittingham G, Pfeffer S, Surovtsev I, Pinglay S, Kennedy K, Schaffer M, Gutierrez J, Sang D, and Poterewicz G (2018). mTORC1 Controls Phase Separation and the Biophysical Properties of the Cytoplasm by Tuning Crowding. Cell.

Dupont S, Morsut L, Aragona M, Enzo E, Giulitti S, Cordenonsi M, Zanconato F, Le Digabel J, Forcato M, and Bicciato S (2011). Role of YAP/TAZ in mechanotransduction. Nature 474, 179–183. [PubMed: 21654799]

Eagen KP, Hartl TA, and Kornberg RD (2015). Stable chromosome condensation revealed by chromosome conformation capture. Cell 163, 934–946. [PubMed: 26544940]

Ellis RJ (2001). Macromolecular crowding: obvious but underappreciated. Trends in biochemical sciences 26, 597–604. [PubMed: 11590012]

Farin HF, Jordens I, Mosa MH, Basak O, Korving J, Tauriello DV, de Punder K, Angers S, Peters PJ, and Maurice MM (2016). Visualization of a short-range Wnt gradient in the intestinal stem-cell niche. Nature.

Fernandez-Sanchez ME, Barbier S, Whitehead J, Béalle G, Michel A, Latorre-Ossa H, Rey C, Fouassier L, Claperon A, and Brullé L (2015). Mechanical induction of the tumorigenic β-catenin pathway by tumour growth pressure. Nature 523, 92–95. [PubMed: 25970250]

Fiedler M, Mendoza-Topaz C, Rutherford TJ, Mieszczanek J, and Bienz M (2011). Dishevelled interacts with the DIX domain polymerization interface of Axin to interfere with its function in down-regulating β-catenin. Proceedings of the national Academy of Sciences 108, 1937–1942.

Fodde R, Smits R, and Clevers H (2001). APC, signal transduction and genetic instability in colorectal cancer. Nature Reviews Cancer 1, 55–67. [PubMed: 11900252]

Gammons M, and Bienz M (2018). Multiprotein complexes governing Wnt signal transduction. Current opinion in cell biology 51, 42–49. [PubMed: 29153704]

Gammons MV, Renko M, Johnson CM, Rutherford TJ, and Bienz M (2016a). Wnt signalosome assembly by DEP domain swapping of Dishevelled. Molecular cell 64, 92–104. [PubMed: 27692984]

Gammons MV, Rutherford TJ, Steinhart Z, Angers S, and Bienz M (2016b). Essential role of the Dishevelled DEP domain in a Wnt-dependent human-cell-based complementation assay. J Cell Sci 129, 3892–3902. [PubMed: 27744318]

Gjorevski N (2016). Designer matrices for intestinal stem cell and organoid culture. Nature 539, 560–564. [PubMed: 27851739]

Guo M, Ehrlicher AJ, Jensen MH, Renz M, Moore JR, Goldman RD, Lippincott-Schwartz J, Mackintosh FC, and Weitz DA (2014). Probing the stochastic, motor-driven properties of the cytoplasm using force spectrum microscopy. Cell 158, 822–832. [PubMed: 25126787]

Guo M, Pegoraro AF, Mao A, Zhou EH, Arany PR, Han Y, Burnette DT, Jensen MH, Kasza KE, and Moore JR (2017). Cell volume change through water efflux impacts cell stiffness and stem cell fate. Proceedings of the National Academy of Sciences, 201705179.

Gutmann R, Leunig M, Feyh J, Goetz AE, Messmer K, Kastenbauer E, and Jain RK (1992). Interstitial hypertension in head and neck tumors in patients: correlation with tumor size. Cancer research 52, 1993–1995. [PubMed: 1551128]

Han YL, Pegoraro AF, Li H, Li K, Yuan Y, Xu G, Gu Z, Sun J, Hao Y, and Gupta SK (2019). Cell swelling, softening and invasion in a three-dimensional breast cancer model. Nature Physics, 1–8.

Hansen MM, Meijer LH, Spruijt E, Maas RJ, Roquelles MV, Groen J, Heus HA, and Huck WT (2016). Macromolecular crowding develops heterogeneous environments of gene expression in picoliter droplets. Nature nanotechnology 11, 191.

Heldin C-H, Rubin K, Pietras K, and Östman A (2004). High interstitial fluid pressure—an obstacle in cancer therapy. Nature Reviews Cancer 4, 806. [PubMed: 15510161]

Horst D, Chen J, Morikawa T, Ogino S, Kirchner T, and Shivdasani RA (2012). Differential WNT activity in colorectal cancer confers limited tumorigenic potential and is regulated by MAPK signaling. Cancer research 72, 1547–1556. [PubMed: 22318865]

Hu J, Jafari S, Han Y, Grodzinsky AJ, Cai S, and Guo M (2017). Size -and speed-dependent mechanical behavior in living mammalian cytoplasm. Proceedings of the national Academy of Sciences 114, 9529–9534.

Hu J, Li Y, Hao Y, Zheng T, Gupta SK, Parada GA, Wu H, Lin S, Wang S, and Zhao X (2019). High stretchability, strength, and toughness of living cells enabled by hyperelastic vimentin intermediate filaments. Proceedings of the national Academy of Sciences 116, 17175–17180.

Jiang J, Tang S, Xia J, Wen J, Chen S, Shu X, Huen MS, and Deng Y (2018). C9orf140, a novel Axin1-interacting protein, mediates the negative feedback loop of Wnt/β-catenin signaling. Oncogene 37, 2992. [PubMed: 29531269]

Johansson J, Naszai M, Hodder MC, Pickering KA, Miller BW, Ridgway RA, Yu Y, Peschard P, Brachmann S, and Campbell AD (2019). RAL GTPases drive intestinal stem cell function and regeneration through internalization of WNT signalosomes. Cell stem cell 24, 592–607. e597. [PubMed: 30853556]

Jun Y, Tripathy SK, Narayanareddy BR, Mattson-Hoss MK, and Gross SP (2014). Calibration of optical tweezers for in vivo force measurements: How do different approaches compare? Biophysical journal 107, 1474–1484. [PubMed: 25229154]

Kim S-E, Huang H, Zhao M, Zhang X, Zhang A, Semonov MV, MacDonald BT, Zhang X, Abreu JG, and Peng L (2013). Wnt stabilization of β-catenin reveals principles for morphogen receptor-scaffold assemblies. Science 340, 867–870. [PubMed: 23579495]

Kishida M, Hino S. i., Michiue T, Yamamoto H, Kishida S, Fukui A, Asashima M, and Kikuchi A (2001). Synergistic activation of the Wnt signaling pathway by Dvl and casein kinase Iε. Journal of Biological Chemistry 276, 33147–33155.

Kishida S, Yamamoto H, Hino S.-i., Ikeda S, Kishida M, and Kikuchi A (1999). DIX domains of Dvl and Axin are necessary for protein interactions and their ability to regulate β-catenin stability. Molecular and cellular biology 19, 4414–4422. [PubMed: 10330181]

Lee WC, Shi H, Poon Z, Nyan LM, Kaushik T, Shivashankar G, Chan JK, Lim CT, Han J, and Van Vliet KJ (2014). Multivariate biophysical markers predictive of mesenchymal stromal cell multipotency. Proceedings of the national Academy of Sciences 111, E4409–E4418.

Li Y, Mao AS, Seo BR, Zhao X, Gupta SK, Chen M, Han YL, Shih T-Y, Mooney DJ, and Guo M (2020). Compression-induced dedifferentiation of adipocytes promotes tumor progression. Science advances 6, eaax5611. [PubMed: 32010780]

Madrzak J, Fiedler M, Johnson CM, Ewan R, Knebel A, Bienz M, and Chin JW (2015). Ubiquitination of the Dishevelled DIX domain blocks its head-to-tail polymerization. Nature communications 6, 6718.

Major MB, Camp ND, Berndt JD, Yi X, Goldenberg SJ, Hubbert C, Biechele TL, Gingras A-C, Zheng N, and MacCoss MJ (2007). Wilms tumor suppressor WTX negatively regulates WNT/ß-catenin signaling. Science 316, 1043–1046. [PubMed: 17510365]

Marshman E, Booth C, and Potten CS (2002). The intestinal epithelial stem cell. Bioessays 24, 91–98. [PubMed: 11782954]

McManus EJ, Sakamoto K, Armit LJ, Ronaldson L, Shpiro N, Marquez R, and Alessi DR (2005). Role that phosphorylation of GSK3 plays in insulin and Wnt signalling defined by knockin analysis. The EMBO journal 24, 1571–1583. [PubMed: 15791206]

Meerbrey KL, Hu G, Kessler JD, Roarty K, Li MZ, Fang JE, Herschkowitz JI, Burrows AE, Ciccia A, and Sun T (2011). The pINDUCER lentiviral toolkit for inducible RNA interference in vitro and in vivo. Proceedings of the national Academy of Sciences 108, 3665–3670.

Metcalfe C, and Bienz M (2011). Inhibition of GSK3 by Wnt signalling–two contrasting models. J Cell Sci 124, 3537–3544. [PubMed: 22083140]

Metcalfe C, Mendoza-Topaz C, Mieszczanek J, and Bienz M (2010). Stability elements in the LRP6 cytoplasmic tail confer efficient signalling upon DIX-dependent polymerization. J Cell Sci 123, 1588–1599. [PubMed: 20388731]

Miyoshi H, and Stappenbeck TS (2013). In vitro expansion and genetic modification of gastrointestinal stem cells in spheroid culture. Nature protocols 8, 2471. [PubMed: 24232249]

Morin PJ, Sparks AB, Korinek V, Barker N, Clevers H, Vogelstein B, and Kinzler KW (1997). Activation of β-catenin-Tcf signaling in colon cancer by mutations in β-catenin or APC. Science 275, 1787–1790. [PubMed: 9065402]

Nelson WJ, and Nusse R (2004). Convergence of Wnt, ß-catenin, and cadherin pathways. Science 303, 1483–1487. [PubMed: 15001769]

Netti PA, Baxter LT, Boucher Y, Skalak R, and Jain RK (1995). Time-dependent behavior of interstitial fluid pressure in solid tumors: implications for drug delivery. Cancer research 55, 5451–5458. [PubMed: 7585615]

Oakes PW, Banerjee S, Marchetti MC, and Gardel ML (2014). Geometry regulates traction stresses in adherent cells. Biophysical journal 107, 825–833. [PubMed: 25140417]

Overduin J, Tylee TS, Frayo RS, and Cummings DE (2014). Hyperosmolarity in the small intestine contributes to postprandial ghrelin suppression. American Journal of Physiology-Gastrointestinal and Liver Physiology 306, G1108–G1116. [PubMed: 24789208]

Pelham RJ, and Wang Y.-l. (1997). Cell locomotion and focal adhesions are regulated by substrate flexibility. Proceedings of the national Academy of Sciences 94, 13661–13665.

Samuel MS, Lopez JI, McGhee EJ, Croft DR, Strachan D, Timpson P, Munro J, Schröder E, Zhou J, and Brunton VG (2011). Actomyosin-mediated cellular tension drives increased tissue stiffness and β-catenin activation to induce epidermal hyperplasia and tumor growth. Cancer cell 19, 776–791. [PubMed: 21665151]

Sato T, and Clevers H (2013). Growing self-organizing mini-guts from a single intestinal stem cell: mechanism and applications. Science 340, 1190–1194. [PubMed: 23744940]

Sato T, Vries RG, Snippert HJ, Van de Wetering M, Barker N, Stange DE, Van Es JH, Abo A, Kujala P, and Peters PJ (2009). Single Lgr5 stem cells build crypt villus structures in vitro without a mesenchymal niche. Nature 459, 262–265. [PubMed: 19329995]

Schwarz-Romond T, Fiedler M, Shibata N, Butler PJG, Kikuchi A, Higuchi Y, and Bienz M (2007). The DIX domain of Dishevelled confers Wnt signaling by dynamic polymerization. Nature structural & molecular biology 14, 484.

Serwane F, Mongera A, Rowghanian P, Kealhofer DA, Lucio AA, Hockenbery ZM, and Campàs O (2017). In vivo quantification of spatially varying mechanical properties in developing tissues. Nature methods 14, 181–186. [PubMed: 27918540]

Shin Y, Berry J, Pannucci N, Haataja MP, Toettcher JE, and Brangwynne CP (2017). Spatiotemporal control of intracellular phase transitions using light-activated optoDroplets. Cell 168, 159–171. e114. [PubMed: 28041848]

Shyer AE, Rodrigues AR, Schroeder GG, Kassianidou E, Kumar S, and Harland RM (2017). Emergent cellular self-organization and mechanosensation initiate follicle pattern in the avian skin. Science 357, 811–815. [PubMed: 28705989]

Snippert HJ, Van Der Flier LG, Sato T, Van Es JH, Van Den Born M, Kroon-Veenboer C, Barker N, Klein AM, Van Rheenen J, and Simons BD (2010). Intestinal crypt homeostasis results from neutral competition between symmetrically dividing Lgr5 stem cells. Cell 143, 134–144. [PubMed: 20887898]

Soofi SS, Last JA, Liliensiek SJ, Nealey PF, and Murphy CJ (2009). The elastic modulus of Matrigel™ as determined by atomic force microscopy. Journal of structural biology 167, 216–219. [PubMed: 19481153]

Stice SL, Strelchenko NS, Keefer CL, and Matthews L (1996). Pluripotent bovine embryonic cell lines direct embryonic development following nuclear transfer. Biology of reproduction 54, 100–110. [PubMed: 8838006]

Strom AR, Emelyanov AV, Mir M, Fyodorov DV, Darzacq X, and Karpen GH (2017). Phase separation drives heterochromatin domain formation. Nature 547, 241. [PubMed: 28636597]

Taelman VF, Dobrowolski R, Plouhinec J-L, Fuentealba LC, Vorwald PP, Gumper I, Sabatini DD, and De Robertis EM (2010). Wnt signaling requires sequestration of glycogen synthase kinase 3 inside multivesicular endosomes. Cell 143, 1136–1148. [PubMed: 21183076]

Tan C, Saurabh S, Bruchez MP, Schwartz R, and LeDuc P (2013). Molecular crowding shapes gene expression in synthetic cellular nanosystems. Nature nanotechnology 8, 602–608.

Tauriello DV, Jordens I, Kirchner K, Slootstra JW, Kruitwagen T, Bouwman BA, Noutsou M, Rüdiger SG, Schwamborn K, and Schambony A (2012). Wnt/β-catenin signaling requires interaction of the Dishevelled DEP domain and C terminus with a discontinuous motif in Frizzled. Proceedings of the national Academy of Sciences 109, E812–E820.

Tee S-Y, Fu J, Chen CS, and Janmey PA (2011). Cell shape and substrate rigidity both regulate cell stiffness. Biophysical journal 100, L25–L27. [PubMed: 21354386]

Thorne CA, Chen IW, Sanman LE, Cobb MH, Wu LF, and Altschuler SJ (2018). Enteroid monolayers reveal an autonomous WNT and BMP circuit controlling intestinal epithelial growth and organization. Developmental cell 44, 624–633. e624. [PubMed: 29503158]

Valenta T, Degirmenci B, Moor AE, Herr P, Zimmerli D, Moor MB, Hausmann G, Cantù C, Aguet M, and Basler K (2016). Wnt ligands secreted by subepithelial mesenchymal cells are essential for the survival of intestinal stem cells and gut homeostasis. Cell reports 15, 911–918. [PubMed: 27117411]

Valnohova J, Kowalski-Jahn M, Sunahara RK, and Schulte G (2018). Functional dissection of the N-terminal extracellular domains of Frizzled 6 reveals their roles for receptor localization and Dishevelled recruitment. Journal of Biological Chemistry 293, 17875–17887.

Van De Wetering M, Sancho E, Verweij C, De Lau W, Oving I, Hurlstone A, Van Der Horn K, Batlle E, Coudreuse D, and Haramis A-P (2002). The β-catenin/TCF-4 complex imposes a crypt progenitor phenotype on colorectal cancer cells. Cell 111, 241–250. [PubMed: 12408868]

Van der Flier LG, Haegebarth A, Stange DE, Van de Wetering M, and Clevers H (2009). OLFM4 is a robust marker for stem cells in human intestine and marks a subset of colorectal cancer cells. Gastroenterology 137, 15–17. [PubMed: 19450592]

van Es JH, Jay P, Gregorieff A, van Gijn ME, Jonkheer S, Hatzis P, Thiele A, van den Born M, Begthel H, and Brabletz T (2005). Wnt signalling induces maturation of Paneth cells in intestinal crypts. Nature cell biology 7, 381–386. [PubMed: 15778706]

Veeman MT, Slusarski DC, Kaykas A, Louie SH, and Moon RT (2003). Zebrafish prickle, a modulator of noncanonical Wnt/Fz signaling, regulates gastrulation movements. Current Biology 13, 680–685. [PubMed: 12699626]

Vinyoles M, Del Valle-Pérez B, Curto J, Viñas-Castells R, Alba-Castellón L, de Herreros AG, and Duñach M (2014). Multivesicular GSK3 sequestration upon Wnt signaling is controlled by p120-catenin/cadherin interaction with LRP5/6. Molecular cell 53, 444–457. [PubMed: 24412065]

Volonté D, Galbiati F, Pestell RG, and Lisanti MP (2001). Cellular Stress Induces the Tyrosine Phosphorylation of Caveolin-1 (Tyr14) via Activation of p38 Mitogen-activated Protein Kinase and c-Src kinase Evidence for caveolae, the actin cytoskeleton, and focal adhesions as mechanical sensors of osmotic stress. Journal of Biological Chemistry 276, 8094–8103.

Wang Y-L, and Pelham RJ (1998). [39] Preparation of a flexible, porous polyacrylamide substrate for mechanical studies of cultured cells. Methods in enzymology 298, 489–496. [PubMed: 9751904]

Weng S, Shao Y, Chen W, and Fu J (2016). Mechanosensitive subcellular rheostasis drives emergent single-cell mechanical homeostasis. Nature materials 15, 961. [PubMed: 27240108]

Whitehead J, Vignjevic D, Fütterer C, Beaurepaire E, Robine S, and Farge E (2008). Mechanical factors activate ß-catenin-dependent oncogene expression in APC1638N/+ mouse colon. HFSP journal 2, 286–294. [PubMed: 19404440]

Wirtz D, Konstantopoulos K, and Searson PC (2011). The physics of cancer: the role of physical interactions and mechanical forces in metastasis. Nature Reviews Cancer 11, 512–522. [PubMed: 21701513]

Xiong F, Ma W, Hiscock TW, Mosaliganti KR, Tentner AR, Brakke KA, Rannou N, Gelas A, Souhait L, and Swinburne IA (2014). Interplay of cell shape and division orientation promotes robust morphogenesis of developing epithelia. Cell 159, 415–427. [PubMed: 25303534]

Yu J, Chia J, Canning CA, Jones CM, Bard FA, and Virshup DM (2014). WLS retrograde transport to the endoplasmic reticulum during Wnt secretion. Developmental cell 29, 277–291. [PubMed: 24768165]

Zeng X, Tamai K, Doble B, Li S, Huang H, Habas R, Okamura H, Woodgett J, and He X (2005). A dual-kinase mechanism for Wnt co-receptor phosphorylation and activation. Nature 438, 873–877. [PubMed: 16341017]

Zhao B, Wei X, Li W, Udan RS, Yang Q, Kim J, Xie J, Ikenoue T, Yu J, and Li L (2007). Inactivation of YAP oncoprotein by the Hippo pathway is involved in cell contact inhibition and tissue growth control. Genes & development 21, 2747–2761. [PubMed: 17974916]

Zhou E, Trepat X, Park C, Lenormand G, Oliver M, Mijailovich S, Hardin C, Weitz D, Butler J, and Fredberg J (2009). Universal behavior of the osmotically compressed cell and its analogy to the colloidal glass transition. Proceedings of the national Academy of Sciences 106, 10632–10637.

Zhou H-X, Rivas G, and Minton AP (2008). Macromolecular crowding and confinement: biochemical, biophysical, and potential physiological consequences. Annu Rev Biophys 37, 375–397. [PubMed: 18573087]

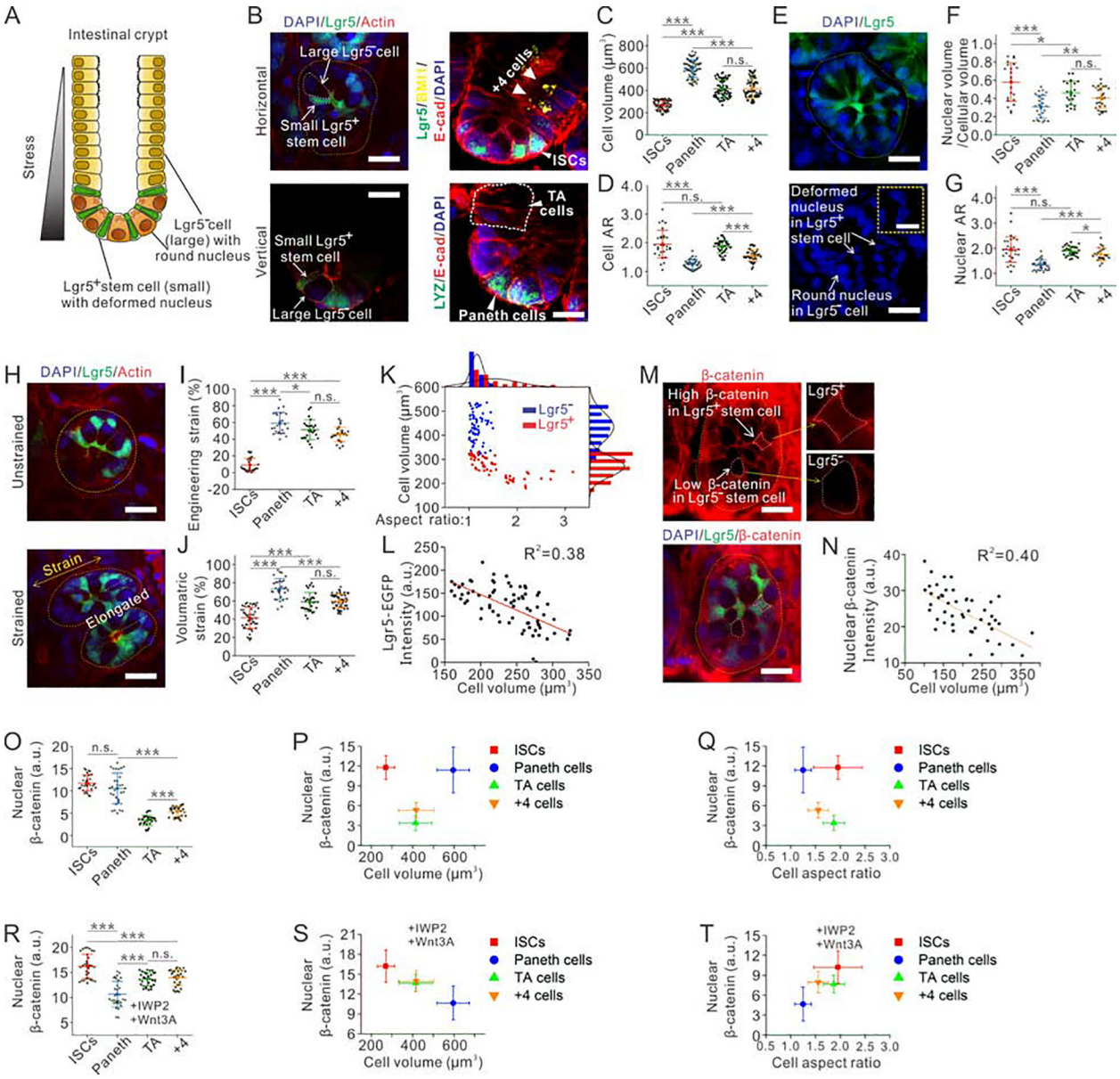

Fig. 1. Distinct physical properties of Lgr5$^+$ stem cells in intestinal crypts correlate with their Lgr5 expression levels.

(A) Schematic illustration of an intestinal crypt.

(B) Immunofluorescent images of an intestinal crypt. Scale bar, 15 μm.

(C-D) Quantitative analysis shows the differences of cell volume (C) and cellular aspect ratio (D) among four different types of cells (ISCs, Paneth cells, TA cells, and +4 cells). n=72 cells from 3 independent experiments for each condition in (C), n=42 cells from 3 independent experiments for each condition in (D).

(E) Immunofluorescent images of intestinal crypts reveal highly deformed nuclei in Lgr5$^+$ stem cells, while nuclei in Lgr5$^-$ cells remain a round shape. Scale baris 10 μm in the image and 5 μm in the inset.

(F-G) Quantitative analysis shows the differences of the nucleus to cell ratio (F) and the nuclear aspect ratio (G) among four different types of cells (ISCs, Paneth cells, TA cells, and +4 cells). n=25 cells from 3 independent experiments for each condition in (F), n=29 cells from 3 independent experiments for each condition in (G).

(H) Immunofluorescent images of intestinal crypts under uniaxial stretch or without stretch. Scale bar, 15 μm.

(I) Quantitative analysis shows different resulted engineering strains among four types of cells (ISCs, Paneth cells, TA cells, and +4 cells) under an applied bulk engineering strain of 70%. n=25 cells for each condition.

(J) Quantitative analysis shows that different resulted volumetric strains under extreme osmotic compression (100% PEG 300) among four types of cells (ISCs, Paneth cells, TA cells, and +4 cells). n=50 cells from 3 independent experiments for each condition.

(K) $Lgr5^+$ stem cells can be distinguished from $Lgr5^-$ cells in the crypt based on their smaller volume and lager aspect ratio. n=71.

(L) The Lgr5 RNA expression level, indicated by Lgr5-GFP intensity, of $Lgr5^+$ stem cells is inversely correlated with the cell volume. n=57.

(M) Immunofluorescent images of intestinal crypts show that $Lgr5^+$ stem cells accumulate more cytosolic β-catenin than $Lgr5^-$ cells. Scale bar, 10 μm.

(N) The amount of nuclear β-catenin in $Lgr5^+$ stem cells is inversely correlated with the cell volume. n=74.

(O) Quantitative analysis shows different amount of nuclear β-catenin among four types of cells (ISCs, Paneth cells, TA cells, and +4 cells). n=30 cells from 3 independent experiments for each condition.

(P-Q) Amount of nuclear β-catenin plotted against cell volume (P) and cell aspect ratio (Q), in all four types of cells in intestinal crypts. n=30 cells from 3 independent experiments for each condition.

(R) Ex vivo cultured intestinal crypts are treated with IWP-2 and Wnt3A ligand. Quantitative analysis shows the different amount of nuclear β-catenin among four types of cells (ISCs, Paneth cells, TA cells, and +4 cells). n=30 cells from 3 independent experiments for each condition.

(S-T) Amount of nuclear β-catenin plotted against cell volume (S) and cell aspect ratio (T) in all four types of cells in intestinal crypts treated with IWP-2 and Wnt3A ligand. The accumulated nuclear β-catenin is negatively correlated with cell volume, while positively correlated with cell aspect ratio. n=30 cells from 3 independent experiments for each condition.

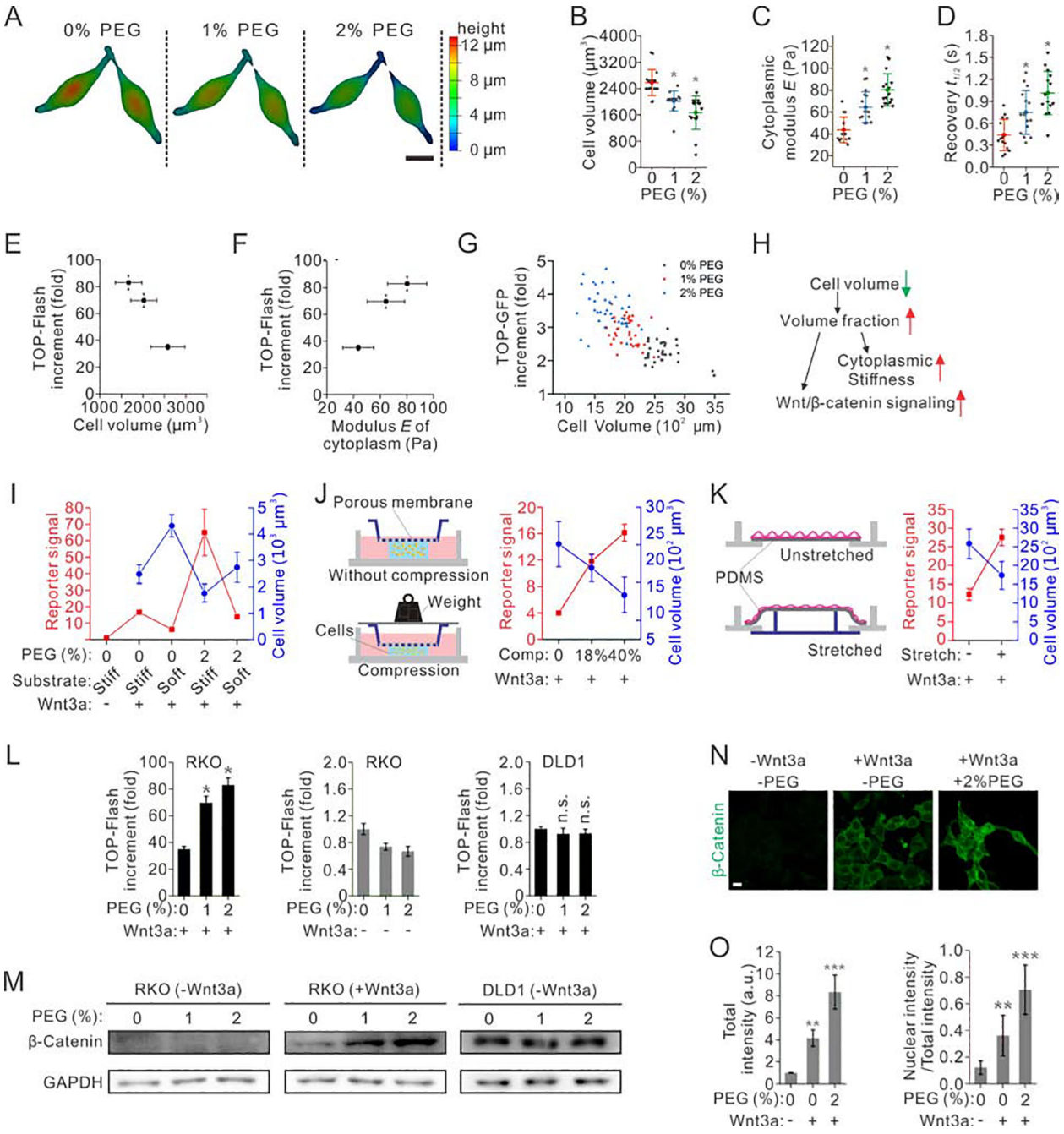

Fig. 2. Physical properties of the cell modulate Wnt/β-catenin signaling.

(A) 3D images of RKO cells under various levels of osmotic compression. Scale bar represents 10 μm. The color scale indicates cell height.

(B) Volume of RKO cells decreases under osmotic compression. n=16 cells.

(C) Stiffness of the cytoplasm of RKO cells increases under osmotic compression, as a result of the increasing crowdedness. n=16 cells.

(D) Fluorescence recovery after photobleaching of Dendra II in RKO cells reveals a significantly increased recovery time under osmotic compression. n=16 cells.

(E-G) Wnt/β-catenin signaling is negatively correlated with cell volume (E), positively correlated with cytoplasm modulus (G) and volume fraction (F). n=16 cells for each condition.

(H) Correlation of multiple physical properties of cells with Wnt/β-catenin signaling. Intracellular crowdedness may serve as a mechanoresponsive regulator of Wnt/β-catenin signaling.

(I) The volume of RKO cells negatively correlates with Wnt/β-catenin signaling under combinations of osmotic compression and substrate stiffness. The substrates were made of polyacrylamide hydrogel, whose stiffness was varied by changing the crosslinker bis-acrylamide concentration.

(J) Schematics of a 3D cell compression device (left). The volume of RKO cells negatively correlates with Wnt/β-catenin signaling under different levels of mechanical compressions (right).

(K) Schematics of a 2D cell stretching device (left). The volume of RKO cells negatively correlates with Wnt/β-catenin signaling under biaxial stretch (right). n=3 for reporter assays, and n=25 for cell volume measurements in (M-O). Individual data points of both TOP-Flash signal and cell volume are derived from n=3 independent experiments, and each of cell volume data contains n=20 cells in (I-K).

(L) Top flash assays of RKO cells with (left) or without Wnt3a ligand (middle), and DLD1 cells with Wnt3a ligand (right) under various levels of osmotic compression. n=3 independent experiments for all conditions.

(M) Western blotting of β-catenin in RKO cells (left without Wnt3a ligand, middle with Wnt3a), and DLD1 cells with Wnt3a ligand (right) under various conditions of compression.

(N) Immunostaining of β-catenin in RKO cells under various conditions of compression. Scale bar, 5 μm.

(O) The level of total β-catenin per cell (left), and the ratio of nuclear β-catenin to total β-catenin (right); both increase under osmotic compression. n=30 cells derived from 3 independent experiments for each condition.

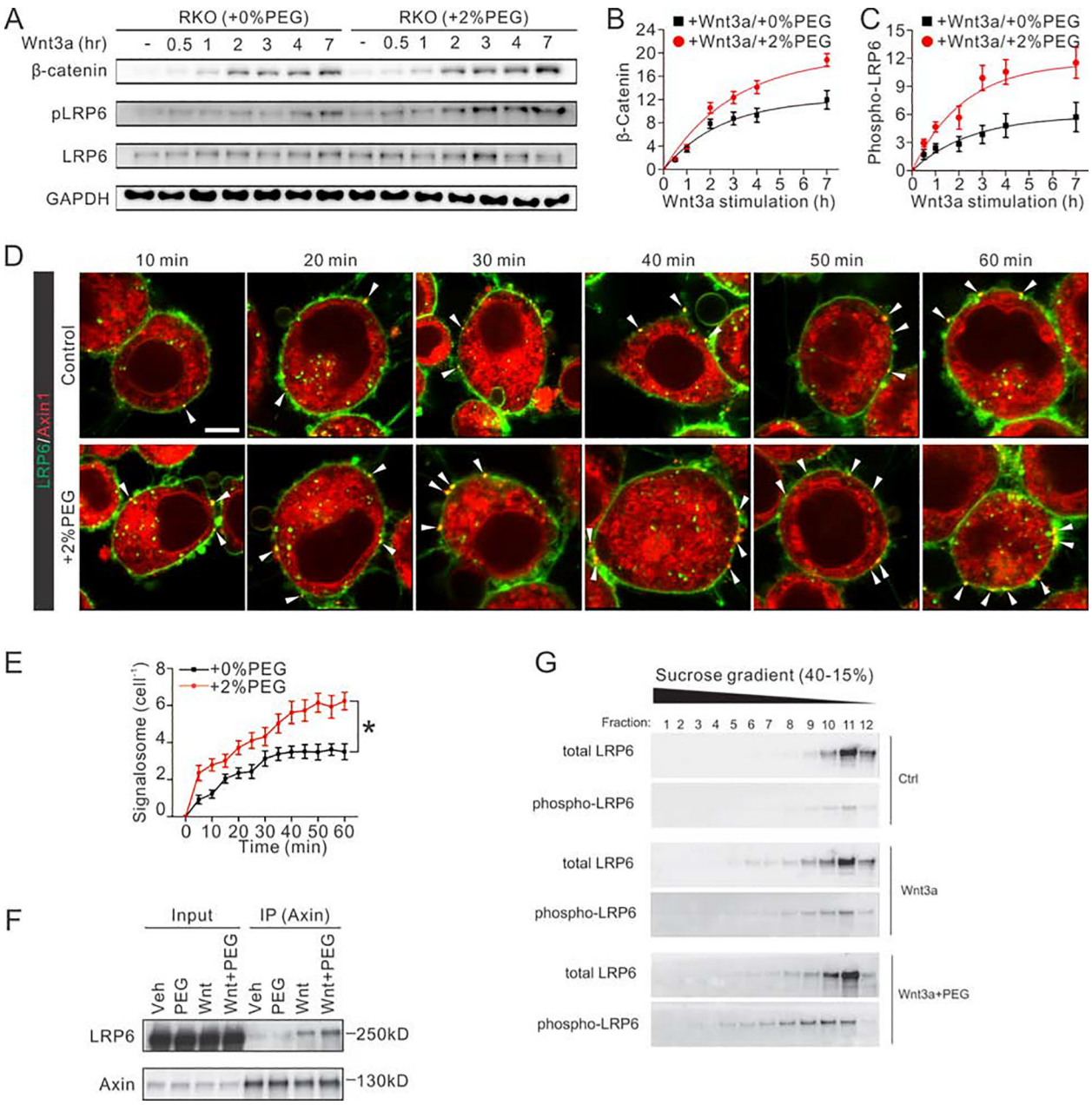

Fig. 3. Intracellular crowding stabilizes β-catenin by promoting formation of the LRP6 receptor signaling complex.

(A) Time dependent accumulation of cytosolic β-catenin and phosphorylation of LRP6 in RKO cells.

(B) Quantifications show that the cytosolic β-catenin accumulates more and faster in cells with osmotic compression. n=3. The relative amount of β-catenin was normalized to GAPDH intensity.

(C) Quantifications show the faster and stronger phosphorylation of LRP6 in cells with compression. n=3. The relative amount of phosphorylated LRP6 was normalized to total LRP6 intensity.

(D) Time-dependent images of LRP6 signalosome formation in RKO cells. Red signal indicates mCherry labeled Axin1, while the green signal indicates the EGFP tagged LRP6. Yellow dots indicate the formation of the LRP6 signalosome. Scale bar, 10 μm.
(E) More LRP6 signalosomes are formed per cell under osmotic compression. n=15 cells derived from 3 independent experiments for each condition.
(F) Lysates of cells with or without osmotic compression were immunoprecipitated with Axin1-specific antibody followed by western blotting analysis of LRP6.
(G) Cells were transfected with FLAG-hLRP6, Mesd, mFz8, hAxin, and GSK3b and treated with control (Con), Wnt3a, or Wnt3a+PEG for 3 hours. Sucrose gradient sedimentation analysis of Triton X-100 lysates of cells. Total and phosphorylated (Tp1479) LRP6 amounts were analyzed by immunoblot.

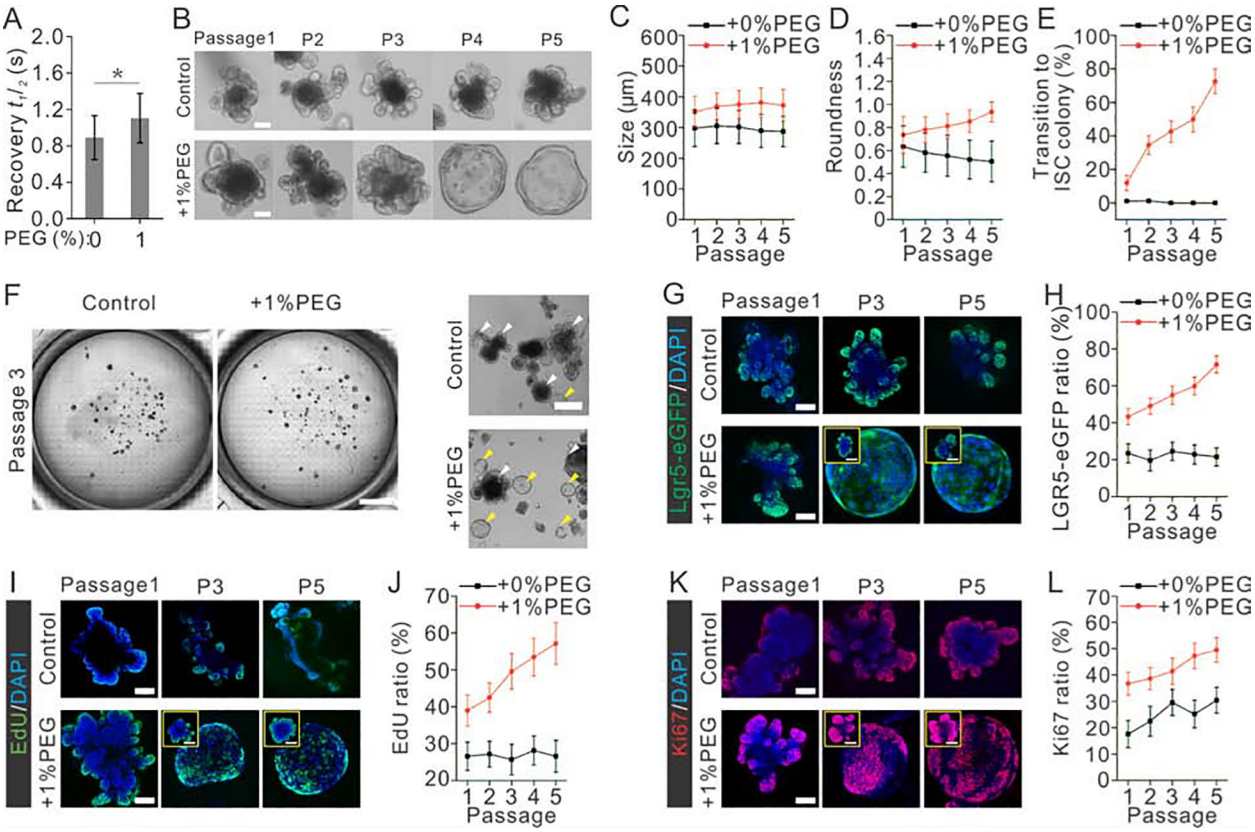

Fig. 4. Compression elevates intracellular crowding, and influences morphology, function and fate of ISCs and expansion of intestinal organoids.

(A) Apparent diffusion of EGFP in the cytoplasm of organoids was measured by FRAP, reflecting the degree of intracellular crowding in the conditions of varying osmotic stress. For each condition, the result is an average of 20 independent experiments.

(B) Images show the typical morphology of organoids cultured with or without compression over 5 passages. Scale bar, 100 μm.

(C-D) Morphology analysis of organoids shows that organoids are becoming rounder and larger under compression over passages. n=30 organoids derived from 3 independent experiments for each condition.

(E) Morphology analysis shows that the portion of organoids transiting to ISC colony increases as organoids are passaged under compression over time. n=3 independent experiments for each condition.

(F) Bright-field images of organoids cultured in petri-dishes with or without compression. Wild field images of fields were directly obtained using tile scan function of confocal microscopy. Scale bar, 4 mm (left), 500 μm (right).

(G-H) Images (G) and quantification (H) indicated by Lgr5-eGFP show that the ratio of intestinal stem cells (ISCs) in organoids increases as organoids are passaged under compression.

(I-J) Images (I) and quantification (J) indicated by EdU staining show that the ratio of cells proliferating in organoids increases over passages under compression.

(K-L) Images (K) and quantification (L) indicated by Ki67 staining show that the ratio of cells proliferating in organoids increases over passages under compression. n=15 organoids derived from 3 independent experiments for each condition in H, J and L. Scale bar: 80 μm in F, H and G, 50 μm in insets.

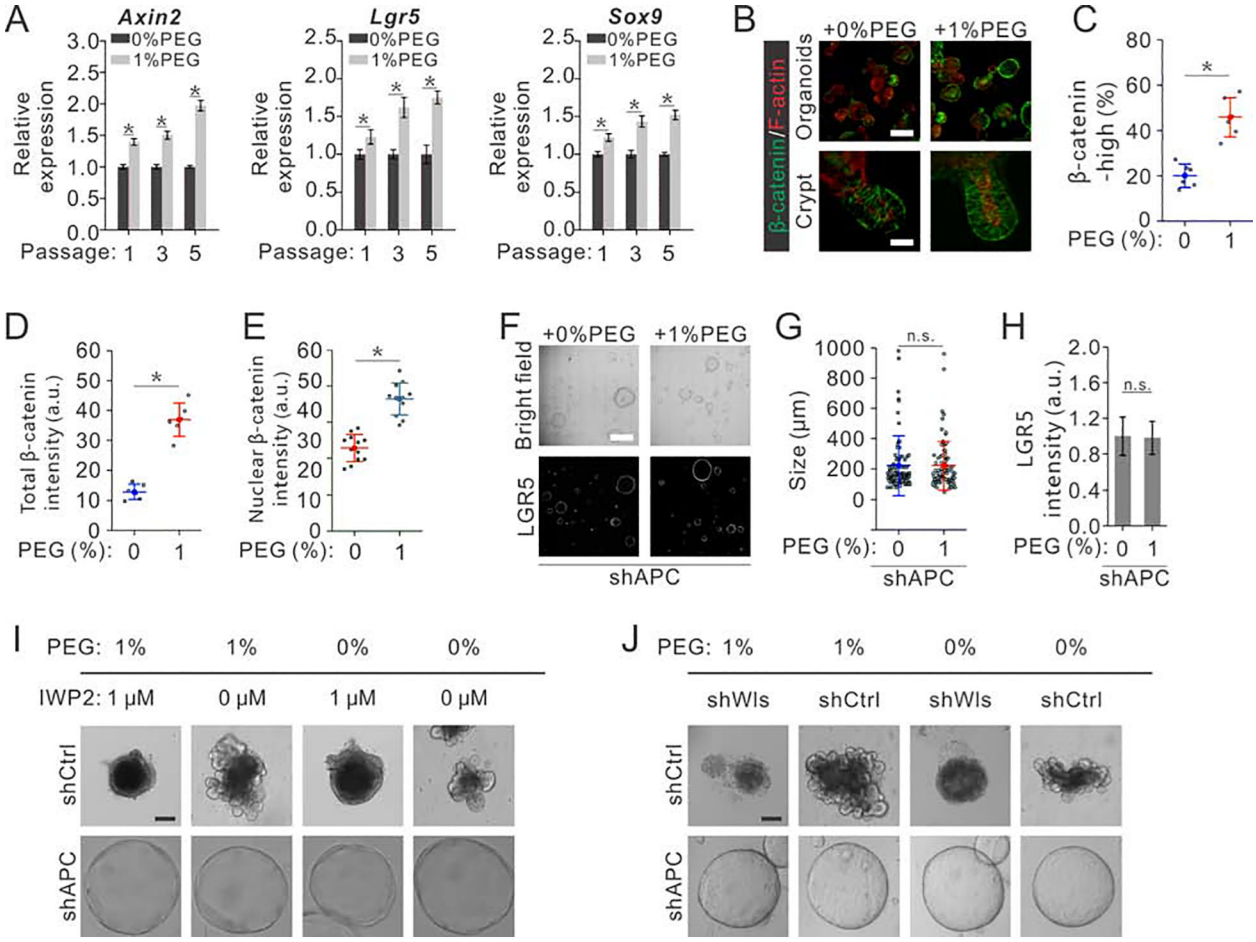

Fig. 5. Compression-mediated intracellular crowding regulates intestinal organoids via Wnt/β-catenin signaling.

(A) qRT-PCR analysis of organoids collected from the 1st, 3rd and 5th passages of intestinal organoids cultured under prolonged compression indicate the elevated Wnt/β-catenin target genes (Axin2, Lgr5 and Sox9). *n*=3 independent experiments for each condition.

(B) Immunostaining of β-catenin in intestinal organoids cultured in hypertonic medium and isotonic medium respectively. Scale bar, 300 μm in top panels, 20 μm in bottom panels.

(C) Quantification shows more β-catenin high expression cells in intestinal organoids cultured in hypertonic medium than in isotonic medium. *n*=6 independent experiments for each conditions.

(D) Quantification shows more total β-catenin accumulated in intestinal organoids cultured in hypertonic medium than in isotonic medium. *n*=6 independent experiments for each conditions.

(E) Quantification shows more nuclear β-catenin accumulated in intestinal organoids cultured in hypertonic medium than in isotonic medium. *n*=6 independent experiments for each conditions.

(F-H) ISCs with Apc depletion exhibit comparable colony forming capabilities (F), comparable sizes (G) and similar stem cell marker Lgr5 expression (H) with or without compression. Images were obtained using tile scan function of confocal microscopy. Scale

bar, 600 μm. *n*=105 organoids derived from 3 independent experiments for each conditions (G); *n*=3 independent experiments for each condition in (H).

(I) Inhibition of Porcupine (endogenous Wnt ligand production) using IWP2 suppresses the growth of intestinal organoids, while increasing intracellular crowding using osmotic compression does not rescue normal organoids growth. As a comparison, IWP2 treatment does not affect the growth of cystic organoids with *APC* depletion. Scale bar, 100 μm.

(J) Inhibition of Porcupine (endogenous Wnt ligand production) using *shWls* suppresses the growth of intestinal organoids, while increasing intracellular crowding using osmotic compression does not rescue normal organoids growth. As a comparison, *shWls* treatment does not affect the growth of cystic organoids with *APC* depletion. Scale bar, 100 μm.

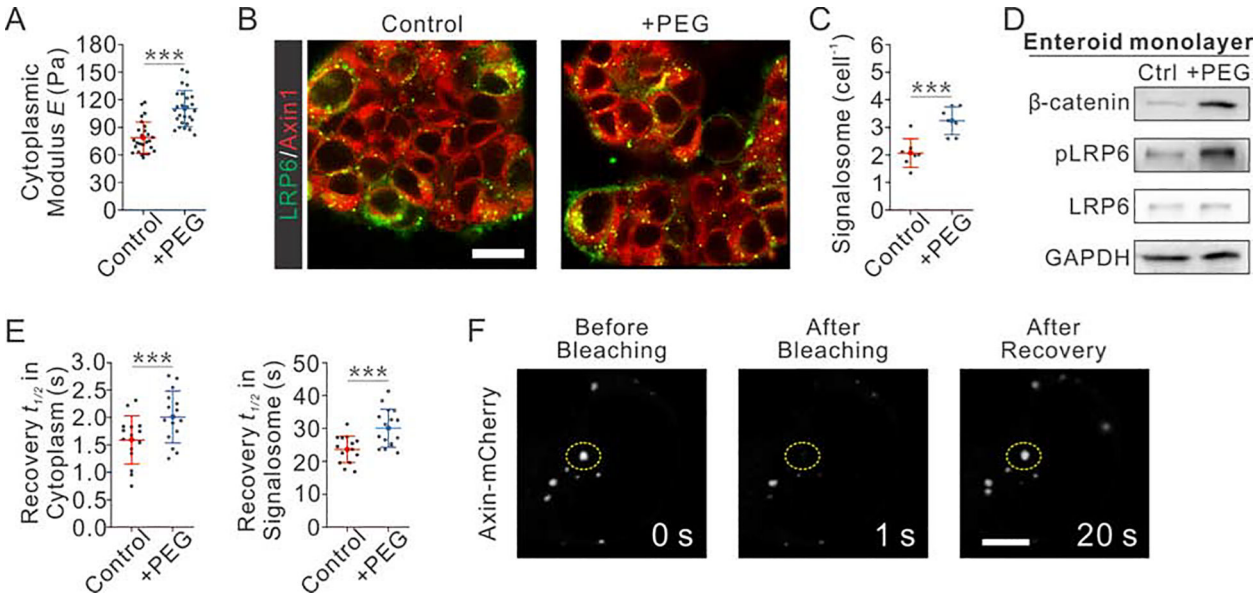

Fig. 6. Volumetric compression modulates Wnt/β-catenin signaling and LRP6-Axin signalosome formation in 2D enteroid monolayers

(A) Volumetric compression increases the cytoplasmic stiffness of cells in 2D enteroid monolayers. *n*= 26 cells from 3 independent experiments for each condition.

(B-C) Images (B) and quantifications (C) show that the osmotic compression increases the number of signalosome formed per cell in enteroid monolayers. *n*=7 independent experiments for each condition, each contains n=35 cells measurements.

(D) Osmotic compression increases the active β-catenin accumulation, and the phosphorylation of LRP6 in 2D enteroid monolayers.

(E) Osmotic compression increases the crowdedness of cytosolic Axin, as shown by the decreased recovery efficiency of cytosolic Axin after bleaching (Left); osmotic compression stabilizes the formation of Axin in signalosome, as shown by the decreased recovery efficiency of Axin in signalosome after bleaching. *n*=15 independent experiments for each condition.

(F) Images show the recovery of Axin in signalosome after photo-bleaching. Scale bar, 4 μm.

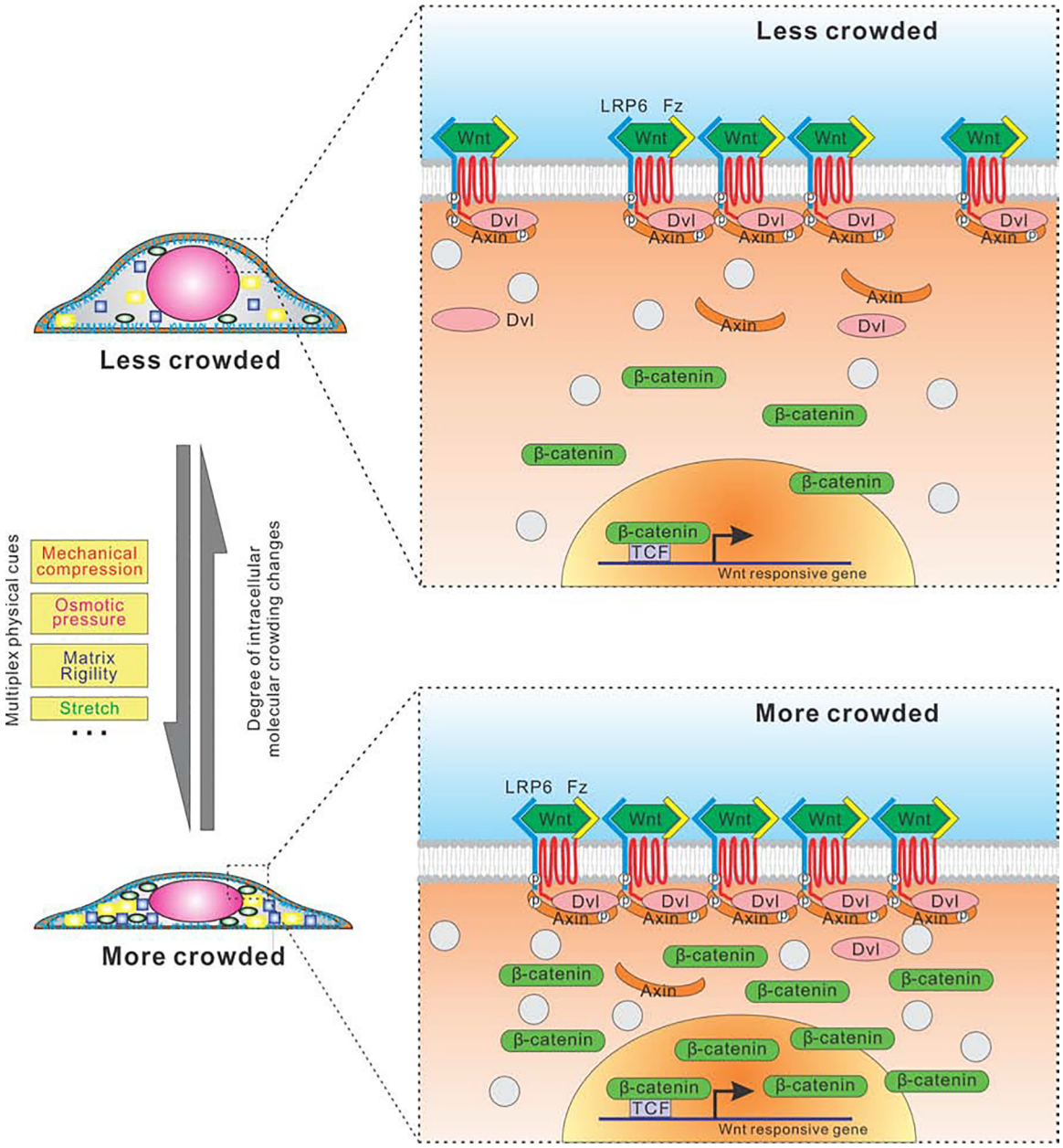

Fig. 7.

A working hypothesis and schematic illustration of how cell interior crowding enhances formation of the LRP6 receptor signaling complex/signalosome.

KEY RESOURCES TABLE

REAGENT or RESOURCE	SOURCE	IDENTIFIER
Antibodies		
Anti-Wnt3a antibody	abcam	ab28472
Anti-Lysozyme antibody	Dako	A0099
Anti-β-catenin antibody	Cell Signaling	Cat#8480
Anti-LRP6 antibody	Cell Signaling	Cat#3395
Anti-LRP6 antibody	Abnova	T1479
Anti-Axin1 antibody	Cell Signaling	Cat#2087
Anti-Axin1 antibody	Millipore	06-1049
Anti-Dvl2 antibody	Cell Signaling	Cat#3216S
Anti-LGR5 antibody	R&D SYSTEMS	Cat#FAB8240P
Anti-GAPDH antibody	Cell Signaling	Cat#5174
Anti-Pho-LRP6 antibody	Cell Signaling	Cat#2568
Anti-Ki67 antibody	Cell Signaling	Cat#9129
Anti-VSV-G tag antibody	abcam	ab1874
Anti-FLAG® antibody	Millipore	F7425
Anti-phospho-Axin (S497/500)	Xi He Laboratory	N/A
Anti-Non-phospho (Active) β-Catenin (Ser33/37/Thr41) antibody	Cell Signaling	Cat# 8814S
Anti-Phospho-β-Catenin (Ser33/37/Thr41) antibody	Cell Signaling	Cat#9561
Anti-Phospho-β-Catenin (Ser45) Antibody	Cell Signaling	Cat#9564
Anti-Bmi1 antibody	Cell Signaling	Cat#5856
Alexa Fluor 488 goat anti-mouse IgG (H+L)	Thermo Fisher scientific	A11029, RRID: AB_2534088
Alexa Fluor 488 donkey anti-rabbit IgG (H+L)	Thermo Fisher scientific	A21206, RRID: AB_2535792
Alexa Fluor 488 donkey anti-goat IgG (H+L)	Thermo Fisher scientific	A11055, RRID: AB_2534102
Alexa Fluor 568 goat anti-rabbit IgG (H+L)	Thermo Fisher scientific	A11036, RRID: AB_10563566
Alexa Fluor 647 donkey anti-rabbit IgG (H+L)	Thermo Fisher scientific	A31573, RRID: AB_2536183
AlexaFluor 647 donkey anti-mouse IgG (H+L)	Thermo Fisher scientific	A31571, RRID: AB_162542
Alexa Fluor 647 goat anti-rat IgG (H+L)	Thermo Fisher scientific	A21247, RRID: AB_10563568
Bacterial and Virus Strains		
E. coli NEB® 5-alpha	New England Biolabs	C2987H
Lentivirus: pInducer 10 shRNA: Non-silencing Control	(Meerbrey et al., 2011)	N/A
Lentivirus: pInducer 10 shRNA: Apc	This paper	N/A
Lentivirus: pGIPZ shRNA: Non-silencing Control	Horizon Discovery	RHS4346
Lentivirus: pGIPZ shRNA: Wls	Horizon Discovery	RMM4532-EG68151
Chemicals, Peptides, and Recombinant Proteins		
Alexa Fluor 647 Phalloidin	Invitrogen	Cat#A22287
CellTracker green CMFDA Dye	Invitrogen	Cat#1546423
Polyethylene glycol 300	Sigma	Cat#1546423

REAGENT or RESOURCE	SOURCE	IDENTIFIER
DAPI	Invitrogen	Cat#D1306
Collagen	Sigma	Cat#5162
Matrigel matrix	Corning	Cat#356232
Nicotinamide	Sigma	Cat#N0636
Y-27632	Sigma	Cat#Y0503
IWP-2	Stemgent	130-105-335
N2 Supplement	Thermo Fisher Scientific	17502-048
50 3 B27 supplement w/o Vitamin A	Thermo Fisher Scientific	12587-010
TGN 020	R&D SYSTEMS	5425
5-Nitro-2-(3-phenylpropylamino)benzoic acid (NPPB)	Sigma-Aldrich	N4779
gadolinium (iii) chloride	Sigma-Aldrich	439770
Critical Commercial Assays		
Click-iT EdU Alexa Fluor 488 Imaging Kit	Invitrogen	Cat#C10337
Dual-Luciferase Reporter Assay System	Promega	Cat#E1960
Experimental Models: Cell Lines		
Human: RKO cells	ATCC	CRL-2577
Human: DLD1 cells	ATCC	CCL-221
Human: HEK293T cells	ATCC	CRL-11268
Mouse: L cells	ATCC	CRL-2648
Mouse: L Wnt3A cells	ATCC	CRL-2647
Human: SW480 cells	ATCC	CCL-228
Human: Ls174T cells	ATCC	CL-188
Experimental Models: Organism/Strains		
C57BL/6J mice	Jackson Laboratory	Stock No: 000664
Lgr5-GFP-IRES-CreER2	Jackson Laboratory	Stock No: 008875
Olfm4-IRES-eGFPCreERT2	(Van der Flier et al., 2009)	N/A
Software and Algorithms		
MATLAB	MathWorks, Natick	N/A
ImageJ	NIH, Bethesda	N/A
Cell volume algorithm	(Guo et al., 2017)	N/A
Oligonucleotides		
Primers for qRT-PCR, see Table S1	This paper	N/A
Recombinant DNA		
pEGFP-N3/hLRP6	Xi He Laboratory	N/A
pCS2+/Flag-hLRP6	Xi He Laboratory	N/A
pcDNA3.1(+)/mAxin1-mCherry	Xi He Laboratory	N/A
Mesd	Xi He Laboratory	N/A
mFz8	Xi He Laboratory	N/A
hAxin	Xi He Laboratory	N/A

REAGENT or RESOURCE	SOURCE	IDENTIFIER
hGSK3β	Xi He Laboratory	N/A
LRP6m5	Xi He Laboratory	N/A
LRP6m10	Xi He Laboratory	N/A
FlagAxinΔDIX,	Xi He Laboratory	N/A
M50 Super 8xTopflash	Addgene	(Veeman et al., 2003), #12456
pRL-TK/Renilla	Promega	E2331
8xGTIIC-luciferase	Addgene	(Dupont et al., 2011), #34615
YAP	Prof. Guan	(Zhao et al., 2007)
Flag-β-catenin	Xi He Laboratory	N/A
Flag-Dvl2	Xi He Laboratory	N/A
shApc	Xi He Laboratory	N/A
shWls	Xi He Laboratory	N/A
TOP-GFP	Addgen	(Horst et al., 2012). #34589
pInducer10-mir-RUP-PheS	Addgene	(Meerbrey et al., 2011). #44011